A Novel Definition of Climate State Using Kalman Filtering and Application to Thresholds

J. Matthew Nicklas,[a] Baylor Fox-Kemper,[a] Charles Lawrence.[a]

[a] *Brown University, Providence, Rhode Island.*

Corresponding author: J. Matthew Nicklas, john_nicklas@brown.edu

ABSTRACT

Herein we present the Energy Balance Model – Kalman Filter (EBM-Kalman), a hybrid model of the global mean surface temperature (GMST), which combines a theoretical energy balance equation based in Earth science literature and a statistical extended Kalman Filter incorporating observed and/or climate model simulated GMST data. This synthesis is possible because climate models and historical temperatures follow easily representable normal distributions due to dynamic instability. A Kalman filter is a powerful, fast tool which assumes normal distributions at each time point, and combines a forward projection given by the energy balance equation with the measured GMST in a weighted average. This model generates an estimate of the 30-year time-averaged climate state but can do so instantaneously: without a lag time of 15 years. It can also determine reasonable probabilities that the climate has crossed a particular threshold or expand the statistical spread of a few computationally intensive simulations of the global climate to estimate an entire ensemble.

SIGNIFICANCE STATEMENT

The overall shape of the Earth's historical climate over the past 150 years can be explained by thermal/light physics equations involving ~12 constants, atmospheric CO2, and volcanic eruptions. Global mean surface temperature measurements vary around this climate state within a consistent distribution. These two observations allowed us to construct a simple model that can estimate Earth’s current climate and aid in policy discussions of climate thresholds.

1. Introduction

What is the uncertainty in Earth's climate? From a measurement standpoint, this issue was resolved many decades ago. The instantaneous measurement of global mean surface temperature (GMST) is currently performed with average precision of 0.05°C (max 0.10°C) via arrays of infrared-sensing satellites and ground stations (Susskind, Schmidt et al. 2019), both these datasets extend back to 1981 (Merchant, Embury et al. 2019), and the cyclical yearly fluctuation (due to the lopsided distribution of Earth’s land mass) is easy to smooth with a running annual average. However, this GMST is still a noisy variable, subject to such factors as El Nino events in the tropical Pacific that typically oscillate with a period of 2-7 years (Hu and Fedorov 2017) and volcanic eruptions that may randomly perturb the climate for 1-2 years (Soden, Wetherald et al. 2002). There are also complexities arising from sparse and inconsistently calibrated historical data and paleoproxy interpretations as the record is extended backward in time (Carré, Sachs et al. 2012; Emile-Geay, McKay et al. 2017; Kaufman, McKay et al. 2020; McClelland, Halevy et al. 2021). Internal variability dominates many climate quantities in the short-term and is much larger than many climate forcing signals, both in climate simulations and reality. (Kirtman, Power et al. 2013; Marotzke and Forster 2015; Gulev, Thorne et al. 2021; Lee, Marotzke et al. 2021) Variables other than GMST, such as Ocean Heat Content Anomaly where >90% of the anthropogenic energy anomaly is found, reveal that the earth’s thermal energy is steadily warming (Gulev et al. 2021; Fox-Kemper et al. 2021), but some smoothing or filtering is required to uncover anthropogenic climate change in the GMST record.

In 1935 the World Meteorological Association began reporting the "standard climate normal" as discrete averages of the global temperatures measured over an interval of 30 years ($\overline{_{30}T}$, starting with 1901-1930), precisely to address the detection of climate change over internal variability and measurement uncertainties in the GMST record. (Guttman 1989) The World Meteorological Association later began updating the 30-year interval every 10 years. A 30-year window is sufficiently long to minimize most fluctuations from climate variability modes (such as El Nino) or short-term forcings such as single volcanoes or solar cycles. This averaged global climate is depicted in Figure 1, and it can be easily updated yearly by a running average rather than every decade (Supp. Fig. 1b). While standard climate normals and running averages are straightforward and widely accepted definitions, these metrics reflect the average climate state centered on 15 years ago, and most of the variability contained within recent 30-year periods reflect the anthropogenic warming trend, rather than the variability that the 30-year "standard climate normal" was designed to smooth out.

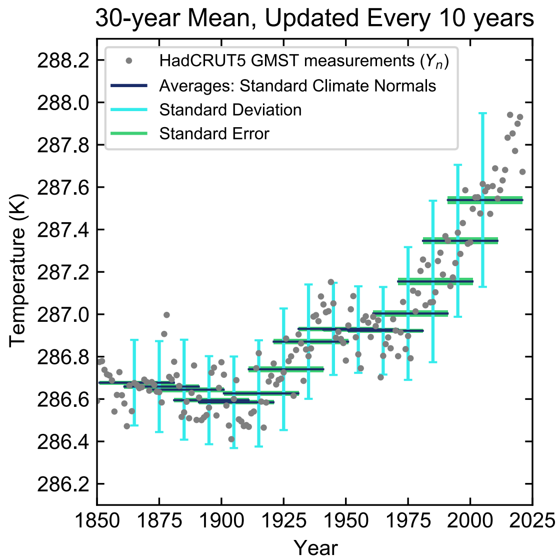

Fig. 1: Illustration of Standard Climate Normals as applied to the HadCRUT5 temperature dataset. (Morice, Kennedy et al. 2021) Note the standard deviation widens considerably due to the considerable increase in temperatures over the 30-year averaging windows in recent decades.

Considering climate policy goals, which often frame decision-making to avoid a particular threshold (e.g., 1.5°C or 2°C above pre-industrial conditions), a 30-year mean implies some difficulty in determining exactly when or if a threshold is crossed (Lee et al. 2021). Tools for assessing the probability that the threshold has been crossed in the past year will be increasingly useful in as these policy targets approach. Relatedly, magnitudes and uncertainty ranges of climate warming must hitherto be attached to specific averaging windows, e.g., "GMST increased by 0.85 [0.69 to 0.95] °C between 1850–1900 and 1995–2014 and by 1.09 [0.95 to 1.20] °C between 1850–1900 and 2011–2020." (Gulev, Thorne et al. 2021). Our method describes the past year's climate system temperature, with uncertainties reflecting the internal variability consistent with the standard 30-year mean.

Mathematically, averaging filters out high-frequency signals that reflect year-to-year variations in global weather, as do other approaches. While moving average filters are good at preserving sudden large sustained changes (such as the anthropogenic change beginning in the mid-1960s in Fig. 1) while removing random noise, other filters or smoothers are better-suited to removing frequencies above a particular cutoff. (Smith 2003) For instance, the Butterworth Smoother has been applied to this global surface temperature time series (Supp. Fig. 1d). (Mann 2008) A sophisticated modification of time-averaging allows for adaptive periods of multiyear averages, known as the optimal climate normal (OCN). (Livezey, Vinnikov et al. 2007). This method utilizes trendlines to determine the number of years to include in each average, with steeper slopes resulting in shorter averaging periods (Supp. Fig. 1c). This OCN is a trade-off: the standard deviation is reduced compared to the standard climate normals in the latter 20th century, whereas the small size of recent averaging periods causes the standard error to increase. Other techniques directly use trendlines. The trendline intervals may be chosen somewhat arbitrarily, say before and after 1975 in the "hinge shape". (Livezey, Vinnikov et al. 2007) Alternatively, Bayesian sequential change point detection may be used to find a probability distribution of the best trendline intervals (Ruggieri and Antonellis 2016) This method takes the climate state as the average of all potential trendlines. (Supp. Fig. 2)

However, climate studies often instead investigate the climate system within coupled climate or earth system models ("coupled" refers to the interaction between multiple sub-models, principally the atmosphere and ocean; (Meehl, Moss et al. 2014)). Typically, these simulations are forced using inputs of historical records and a range of scenarios of future projections (including CO2 emissions, other pollutants, and land use; Lee et al. 2021). Subtle variation of initial conditions can produce a population of identically-forced simulations that through the chaotic nature of weather explore the whole span of the climate system's range of outcomes consistent with that climate forcing, such as for the CESM2 Large Ensemble (Rodgers, Lee et al. 2021), abbreviated here as LENS2. Unfortunately, each ensemble member is computationally expensive, and does not accurately or transparently reflect the real climate system.

Therefore, we have created a model that has both an energy-balance difference equation intended to capture the underlying physics and a statistical observation equation that brings in the available data hybrid physical model-statistical filter. Our model is one example of data-driven climate emulators (Forster, Storelvmo et al. 2021), which by construction contains specific benefits inherited from its chosen constituent models. Our simple iterative energy-balance model contains the major driving physics of the climate system with just 12 coefficients (of which 5 are reducible) and has good skill at predicting the GMST despite being "blind" to all measurements (i.e., a “forward” model in numerical weather prediction terminology). The statistical component is an extended Kalman Filter, which allows for incorporation of current measurements to "course-correct" under a well-understood mathematical framework. Hybridizing these two models yields statistical distributions of uncertainty due to internal variability regarding the current climate state. In other words, it is a simplified data assimilation tool. This combined model can project into the future, transparently driven by climate forcers: CO_2 and volcanic dust. Furthermore, its internal uncertainty approximates the spread of simulation model ensembles (e.g., LENS2). Of course, large ensembles also predict regional variability and changes to components such as subsurface oceans, sea ice, clouds, etc., while this model predicts only GMST.

2. Methods

a. Energy-Balance Model

The energy-balance model is constructed by envisioning a uniform planet and capturing the principal atmospheric and surface energy fluxes (Budyko 1969; Sellers 1969). This model is "blind" with respect to current GMST measurements, and is inspired by the work of other energy-budget models illustrating quantitative skill (Hu and Fedorov 2017; Kravitz, Rasch et al. 2018).

$$\Delta \text{Energy} = \phi_{SW}(\text{in}) - \phi_{LW}(\text{out}) \tag{1}$$

$$\frac{T_{n+1}-T_n}{k} C_{heat} = G_0 * \tilde{d}_n * f_{\alpha A}(T_n) * f_{\alpha S}(T_n) - j^{\star} * \tilde{g}_n * f_{H2O}(T_n) \tag{2}$$

The time unit k is 1 year, matching the time step of this iterative difference equation model. For simplicity, n is taken as the calendar year (e.g., 2000). On the right side of the equation, both the shortwave radiative flux and longwave radiative flux take the same form: (source G_0 , $j^{\star}$) * (prescribed attenuation: $\tilde{d}_n, \tilde{g}_n$) * (feedback attenuation: $f_?(T_n)$). The heat capacity of the whole climate system and land mass on a yearly time scale, C_{heat}, is known with the least precision: reported values are 17 ± 7 W (year) m^{-2} K^{-1}, (Schwartz, 2007). G_0 is the extraterrestrial irradiance at 340 W/m^2, $\tilde{d}_n$ is the prescribed shortwave light attenuation due to volcanic dust, $f_{\alpha A}(T_n)$ is the additional atmospheric shortwave attenuation due to cloud albedo, while $f_{\alpha S}(T_n)$ is the surface shortwave attenuation due to ground albedo. The ideal black body radiation is $j^{\star} = \sigma_{sf} T_n^4$ (also known as Planck feedback), $\tilde{g}_n$ is the prescribed longwave attenuation due to CO_2 scaled to include other greenhouse gasses, and $f_{H2O}(T_n)$ is the additional atmospheric longwave attenuation due to water vapor and other gasses parameterized as a function of GMST. Several of these terms were defined to satisfy the constraints of the climate feedbacks presented in the IPCC's AR6 (Forster et al. 2021; particularly Table 7.10), and all coefficients were based on literature values (full derivation in

Appendix A). The model also assumes a prehistorical (1850) GMST of 286.7K (13.55°C), which allows the 1960-1990 "standard climate normal" to fall within the range given by Jones and Harpham (2013). The two albedo feedbacks are expressed relative to 287.5K, the temperature in 2002.

Overall, this yields a blind (forward) energy-balance model (see the orange dashed line in Figure 2) with 7 irreducible, non-integer coefficients and good skill at predicting the GMST with an $R^2 = 0.88$ in describing the HadCrut5 GMST timeseries (Morice, Kennedy et al. 2021). With only minor modifications, this method could be used with *multiple* annual temperature reconstructions at the same time (e.g. GISTEMP (Lenssen, Schmidt et al. 2019)), considering each as only an estimate of the true GMST. (Willner, Chang et al. 1977)

$$\begin{aligned} T_{n+1} &= T_n + \frac{137.7\text{m}}{AOD_n+9.73\text{m}}\left(1+\frac{T_n-287.5\text{K}}{687.1\text{K}}\right)\left(1+\frac{T_n-287.5\text{K}}{572.6\text{K}}\right) \\ &\quad - \left(\frac{T_n}{274.9\text{K}}\right)^{2.385} \log_{10}\left(\frac{1.893*10^{15}\text{ppm}}{[CO_2]_n}\right) = F(T_n;[CO_2]_n,AOD_n) \end{aligned} \tag{3}$$

$$\begin{aligned} \frac{\partial T_{n+1}}{\partial T_n} &= 1 + \frac{0.4407\text{m}}{AOD_n+9.73\text{m}}\left(1+\frac{T_n-287.5\text{K}}{629.9\text{K}}\right) \\ &\quad - \left(\frac{T_n}{8464.\text{K}}\right)^{1.385} \log_{10}\left(\frac{1.893*10^{15}\text{ppm}}{[CO_2]_n}\right) = \frac{\partial F(T_n;[CO_2]_n,AOD_n)}{\partial T_n} \end{aligned} \tag{4}$$

This function F and the partial derivative of F will become critical parts of the Kalman filter: (6-8) below.

b. EBM-Kalman Filter: A Weighted Average of Energy Balance and Measurements

While similar algorithms were developed in the 1880s by Thorvald Nicolai Thiele (Lauritzen 1981; Lauritzen and Thiele 2002), Kalman filtering rose to prominence due to its use in the Apollo navigation computer as proposed by Ruslan Stratonovich (1959; 1960), Peter Swerling (1959), Rudolf E. Kálmán (1960), Richard S. Bucy (1961), and implemented by Stanley Schmidt (1981). Versions of this statistical filter are universally used in aerospace guidance systems, as well as in a variety of other scientific fields. (Grewal and Andrews 2001) They are also often used in aspects of numerical weather prediction (Annan, Hargreaves et al. 2005), although they are ineffective as the sole data assimilation tool for weather (Bouttier 1996). The Kalman filter can be applied to most situations in which there are noisy measurements of a system with known underlying dynamics.

In-depth derivations and tutorials for constructing Kalman filters have been published elsewhere (Miller 1996; Lacey 1998; Särkkä 2013; Benhamou 2018; Youngjoo and

Hyochoong 2018; Ogorek 2019), although there is no standard symbol convention. Here we provide a basic intuition, using the seminal example of the Apollo spacecraft. Initially, there is some estimated *state vector* (acceleration, velocity, and position vectors) of the craft $\mathbf{\hat{x}_{n-1}}$ and a Gaussian uncertainty envelope around this vector defined by a *state covariance matrix* $\mathbf{P_{n-1}}$. These can be projected a priori into the future using a *dynamic model matrix* $\mathbf{\Phi}$ (for a spacecraft this is from physics, for our climate system this is extended to the function F (7), the energy balance model (3)), and the projected covariance enlarges by an additional assumed *model covariance* $\mathbf{Q}$, yielding $\mathbf{P_{n|n-1}}$ (8). Now a *measurement vector* $\mathbf{y_n}$ is considered (9). The probabilistic range of discrepancies between $\mathbf{\Phi\hat{x}_{n-1}}$ and $\mathbf{y_n}$ is given by the *innovation covariance matrix* $\mathbf{S_n}$, which is the sum of $\mathbf{P_{n|n-1}}$ and an assumed *measurement covariance* $\mathbf{R}$ (10). The *a posteriori estimate* for the state $\mathbf{\hat{x}_n}$ is found by taking a weighted average of $\mathbf{\Phi\hat{x}_{n-1}}$ and $\mathbf{y_n}$ (12), with the weight on $\mathbf{y_n}$ given by $\mathbf{P_{n|n-1}(S_n)}^{-1}$, a product known as the *Kalman gain* (11). To reflect the greater certainty in the state vector because of this correction, $\mathbf{P_n}$, the *a posteriori covariance matrix*, is $\mathbf{P_{n|n-1}}$ shrunk by a factor of ($\mathbf{I}$ minus the Kalman gain (13)). To summarize within the context of Bayesian probability, the *prior distribution* is given by projecting $N(\mathbf{\hat{x}_{n-1}}, \mathbf{P_{n-1}})$ into the future using $\mathbf{\Phi}$, which is multiplied by the support of $\mathbf{y_n}$ to give a *posterior distribution* $N(\mathbf{\hat{x}_n}, \mathbf{P_n})$.

If $\mathbf{y_n}$ is an indirect measurement of the state vector $\mathbf{x_n}$ (for instance Apollo's accelerometers, or GMST approximated by a set of different measurements across the globe), this necessitates an emission / observation matrix $\mathbf{H}$, further complicating the above procedure. For this application to the global climate system, all terms are scalars and the emission matrix $\mathbf{H} = \mathbf{I} = 1$, so we use italicized notation to indicate this case.

$$\Phi_n = \frac{\partial \mathrm{F}(x;u_n)}{\partial x}\Big|_{x=\hat{x}_{n-1}} \quad \text{linearization at timepoint n} \tag{5}$$

$$\begin{cases} x_n = \mathrm{F}(x_{n-1};u_n) + w_n \\ y_n = x_n + v_n \end{cases} \quad \begin{matrix} \text{dynamic model, error:} & \mathrm{Q}=\mathrm{E}[w_n^2] \\ \text{measurements, error:} & \mathrm{R}=\mathrm{E}[v_n^2] \end{matrix} \tag{6}$$

$$\hat{x}_{n|n-1} = \mathrm{F}(\hat{x}_{n-1};u_n) \quad \text{a priori estimated state projection} \tag{7}$$

$$\mathrm{P}_{n|n-1} = \Phi_n^2 \mathrm{P}_{n-1} + \mathrm{Q} \quad \text{a priori state variance projection} \tag{8}$$

$$c_n = y_n - \hat{x}_{n|n-1} \quad \text{innovation residual} \tag{9}$$

$$\mathrm{S}_n = \mathrm{P}_{n|n-1} + \mathrm{R} \quad \text{innovation covariance} \tag{10}$$

$$\mathrm{K}_n = \mathrm{P}_{n|n-1} / \mathrm{S}_n \quad \text{Kalman gain} \tag{11}$$

$$\hat{x}_n = \hat{x}_{n|n-1} + \mathrm{K}_n \mathrm{c}_n \quad \text{a posteriori estimated state} \tag{12}$$

$$P_n=(1-K_n)P_{n|n-1} \qquad \text{a posteriori state covariance} \qquad (13)$$

Returning to the original climate state context of this paper, we are concerned with a one-dimensional GMST, so the equations are for simple scalars rather than matrices and vectors. Here, we take the abstract unknown state x_n to be climate temperature, particularly an underlying GMST capturing only the climate state T_n and not annual weather-pattern related variability in GMST. The noisy measurements Y_n are the yearly time series of GMST measurements, and $\hat{T}_n$ is the estimate of the unknown climate state, both expressed in units of K. The energy-balance model F (3) governing $\hat{T}_n$ is nonlinear (with T^2 and $T^{2.385}$ terms due to albedo and Planck feedbacks), which necessitates an extended Kalman filter (EKF): the a priori estimated state projection is given by (7) above and Φ_n for the a priori state covariance (8) projection is a time-varying linearization (5). This energy-conserving difference equation resembles using a first-order Taylor series approximation of a differential energy-balance model (if discretization errors are considered part of the tendency), or the integral form of a conservative discretization in time (if fluxes on the right side are taken as a model for their time-integrated value), and the Kalman Filter re-approximates a climate state underlying the GMST at every time step. Conveniently, because the derivative of the energy-balance equation does not change significantly over the relevant range of temperatures (286K - 289K), more complex extensions of the Kalman filter, particularly the Unscented Kalman Filter (Julier and Uhlmann 1997; Wan and Van Der Merwe 2000) is not necessary (see Appendix B).

In summary, the extended Kalman filter projects forward one year into the future based on the unbalanced fluxes of the energy balance model equation, and then takes a weighted average of this projection with the annual GMST measurement (the data assimilation increment). Thus, even though the EBM conserves energy (by construction), the combined EBM-Kalman Filter does not, unlike other alternative data assimilation approaches (e.g., (Wunsch and Heimbach 2007)). The state estimates from this EBM-Kalman Filter (in navy blue in Fig. 2) almost always lie between the blind EBM (in dashed orange in Fig. 2) and the annual GMST measurements (scattered gray dots in Fig. 2). It is possible for the EBM-Kalman Filtered state estimates to escape these bounds for a short time, for instance if a series of colder years shift the EBM-Kalman Filtered state estimate below the blind EBM, and then the next GMST measurement is slightly warmer than the blind EBM (e.g., from 1937 to 1939 in Fig. 2). While the EBM within the EKF projects warming, this imbalance does not resolve within a single year due to heat capacity and the new observation does not raise the weighted average by much, so the EKF state estimate is colder than both.

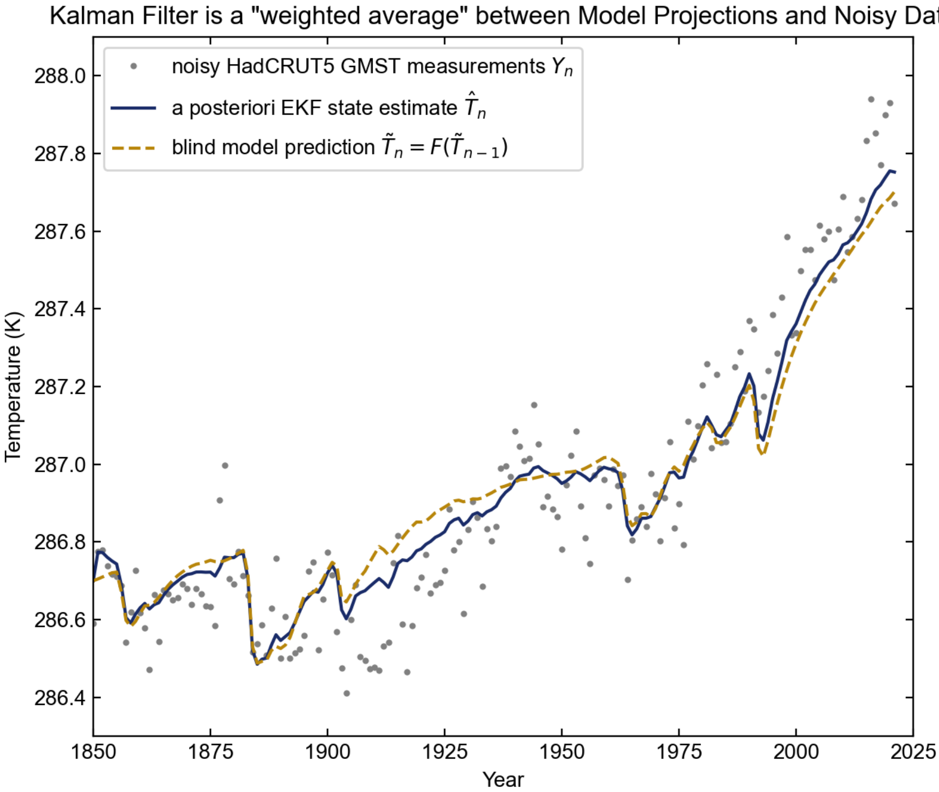

Fig. 2: Depiction of the Kalman Filter's underlying mechanism. The blind energy-balance model prediction is drawn in dashed orange. The Kalman Filter state estimate in navy blue uses these energy-balance dynamics to project from the previous state to the current state. The measured GMST (gray dots - Hadcrut5) pull the Kalman Filter state estimate toward it with a small weight. Note that the $r^2 = 0.88$ is higher for the HadCRUT5 dataset than HadCRUT4 (Morice, Kennedy et al. 2012), but recent time points the measured GMSTs do not match the model quite as nicely and the blind model undershoots. Other researchers may consider that this may justify tweaking the coefficients (eg yet higher β_0 due to stronger short-term forcings).

In this first version of the EKF shown in Fig. 2, we use a measurement uncertainty R in (10) that is constant and based on the HadCRUT5 variance with respect to its 30-year running mean (0.0111 or standard deviation of 0.105K). The climate model uncertainty, Q, was set to R/30 to tie back to the 30-year running average definition of climate state (Guttman 1989). By this simple method, we have tuned the data-assimilating Kalman filter to model the “standard climate normal”.

3. Results

a. The Historical EBM-Kalman Filtered Climate (1850-Present)

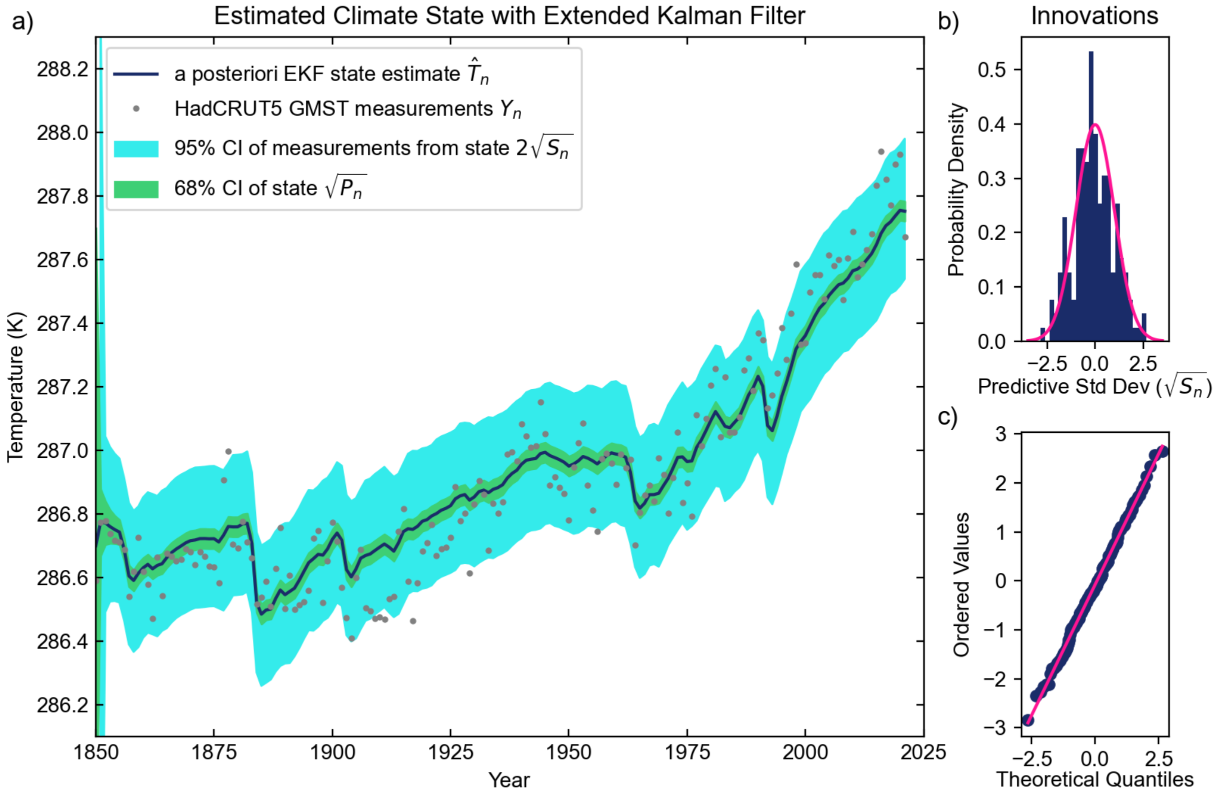

Fig. 3: EBM-Kalman Filter and Associated Uncertainties. a) The Kalman Filter state estimate (navy blue line) is drawn with a $1\sigma = \sqrt{P_n}$ confidence interval (light green area). GMST measurements are again in gray dots. In light blue, a 2σ confidence interval of the innovation covariance ($\sqrt{S_n}$) is drawn around the projected state estimate $\hat{T}_{n|n-1}$, which represents a 95% confidence interval of where the Kalman Filter expects the subsequent year's temperature measurement to be. After an initial convergence period of about a decade, $\sqrt{P_n}$ converges to 0.0307K and $\sqrt{S_n}$ converges to 0.110K. Note that in 2021 the temperature measurement was cooler than the climate state predicted, so while the blue temperature forecast window continues to track warmer with rising CO2, the state estimate is revised down from the projected a priori state. b) The deviation between the projected climate state and measurements, as plotted against the ideal distribution given by the innovation covariance. The empirical and ideal deviation probability distributions closely match, confirming that the annual measurements of GMST can be interpreted as Gaussian noise around an underlying climate state approximating the "standard climate normal" 30-year mean. c) In the qqnorm plot, the innovation data follows a straight line. This shows good support for the Kalman filters's assumption of normal residuals.

The primary product of this paper is the EBM-Kalman Filtered climate state as displayed above in Fig. 3a. We emphasize again that all the mathematical constants in the forward EBM underlying this filter were obtained from published literature values: this is not an empirical fit to the HadCRUT5 GMST data. Within this Kalman filtered climate, there are two distinct Gaussian distributions relevant to climate science: the uncertainty in the current state, as graphed in light green envelope in Fig. 3a, and the window of possible next-year GMST measurements, as graphed in the light blue envelope in Fig 3a. Further examination of the difference between projected states $\hat{T}_{n|n-1}$ and a posteriori estimated states $\hat{T}_n$ reveals that on an individual year basis, assimilation of the GMST measurement only shifts $\hat{T}_{n|n-1}$ by at most 0.025K, compared with the standard deviation of the adjustment in $\tilde{T}_n$ from the blind, forward model contribution of up to 0.05K per year. However, as demonstrated in Figure 2, repeated small increments of this magnitude by consistently lower or higher than expected GMST measurements can push $\hat{T}_n$ away from $\tilde{T}_n$ by as much as 0.08K over a few years. In net over the entire time series, the measurements have nearly equal warming and cooling contributions to the underlying $\hat{T}_n$ climate state, forming the expected Gaussian distribution as demonstrated in Fig 3B. This reveals that the vast amount of change in the underlying climate state can be explained by the literature-based blind, forward energy-balance model and measurements of greenhouse gas and stratospheric aerosol concentrations, consistent with recent forward-EBM applications (Hu and Fedorov 2017; Kravitz, Rasch et al. 2018).

b. Threshold Crossing

An annual measurement is not a measurement of climate change due to the internal variability of the system, and so a single annual temperature above a particular threshold is not a guarantee of the climate state crossing the threshold. We can interpret threshold crossing to reflect when the uncertain climate state (here taken as an estimate of the “standard climate normal”, or 30-year mean temperature) is determined with a given probability to have passed a threshold, or instead could reflect the probability that the possible measurements in the next year will exceed the threshold. This EBM-Kalman Filtered climate product has the convenient ability to generate both GSAT-based probability distributions for whether a threshold has been crossed. Also, both definitions may also be applied to regional climates (with a suitably redefined regional forward model), for instance the former regional threshold crossing definition was investigated by Tebaldi and Knutti (2018).

The IPCC AR6 (Lee, Marotzke et al.) states “the time of GSAT exceedance is determined as the first year at which 21-year running averages of GSAT exceed the given threshold”. This threshold exceedance by the climate state, as in the IPCC definition, is given within the EBM-Kalman Filter by a Gaussian distribution (green in Fig. 4a) about the state $\hat{T}_n$

with a variance given by P_n. The IPCC has an ensemble of models to draw upon over both the historical period and future projections, so the fraction of the 21-year means of each of the ensemble members found above a given threshold determines the overall probability that the climate threshold was crossed (assuming the ensemble spread is a good representation of GMST uncertainty – recent IPCC reports instead widen the ensemble spread to approximate the uncertainty range because coarse climate models under-represent internal variability and model uncertainty: (Lee, Marotzke et al.), Box 4.1). The Kalman filter estimate does not require this future projection, because it provides an instantaneous estimate of the "climate state", and we can take simulated draws from this a posteriori state. In other words, the probability of the "climate state" exceeding the threshold is the cumulative distribution function (with mean μ set to the threshold and variance $\sigma^2 = P_n$) at value of $\hat{T}_n$. Furthermore, the EBM-Kalman Filter climate state covariance reflects the uncertainty in the 30-year average of real-world GMST without empirical retuning.

Regarding the second meaningful interpretation of threshold crossing which we deem "annual temperature forecast" above the threshold, the Kalman framework shows these predictions as the window (blue in Fig. 4b) of possible next-year GMST measurements, a Gaussian distribution centered at the projected state $\hat{T}_{n|n-1}$ with a variance given by the innovation covariance (S_n): in other words, a simulated draw from the a priori state. This uncertainty range reflects and encapsulates the actual real-world GMST measurements (see Fig 3b). For an ensemble of climate models, the analogous "temperature forecast" probability is the fraction of simulations at year x that are warmer than the threshold.

There is additional ambiguity regarding what "crossing a threshold" means regarding any time-varying probability, especially given that due to volcanic eruptions these time-varying probabilities may not monotonically increase (as is the case for a cumulative distribution function). Here we define (based on the 1σ confidence interval, or the *likely* range in IPCC terminology) the "threshold crossing period" to span from the earliest year when ≥15.9% of climate states or temperature forecasts exceed the threshold to the latest year when ≤84.1% of climate states or temperature forecasts exceed that threshold. We can further note a "threshold crossing instant" to be the year(s) when the probability of exceeding the threshold is nearest to 50% if successive years' probabilities cross 50% (or *as likely as not* to have crossed the threshold in IPCC terminology). Regardless of whether a coupled climate model or EBM-Kalman Filter is used, the temperature forecast method has a longer span of threshold crossing period than the climate state because the uncertainty/ensemble spread in the annual forecasts is wider than the uncertainty/ensemble spread of the time-averaged states, and both methods report similar threshold crossing instants (see Fig. 9).

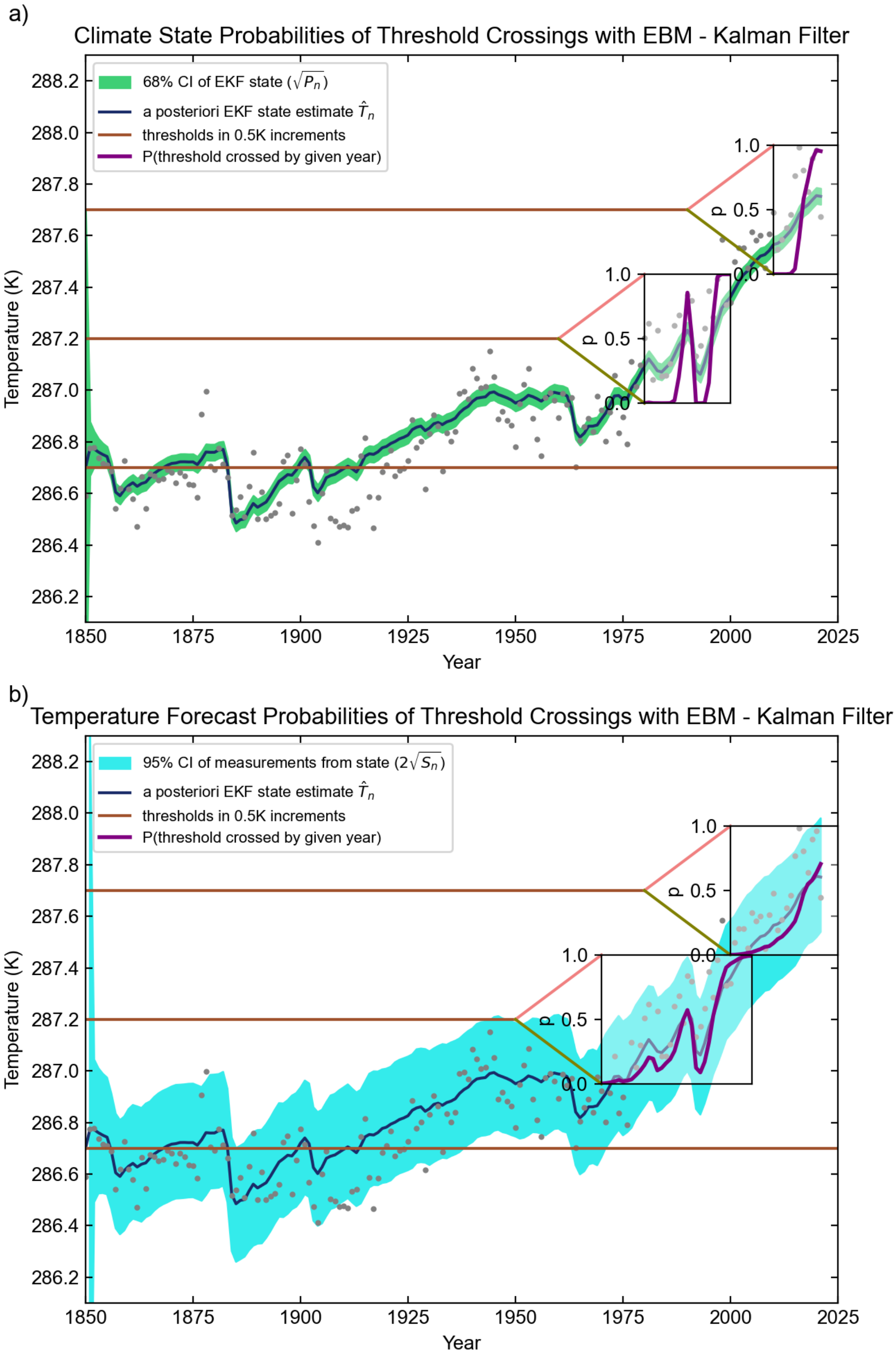

Fig. 4: a) EBM-Kalman Filter and Climate State Thresholds: As in Fig. 3, there is the EBM-Kalman Filtered state estimate (navy blue line), a 1σ confidence interval of the model state covariance (P_n) in green blue, and GMST measurements in gray dots. Additionally, there are 3 horizontal brown lines at 286.7K (the pre-industrial climate temperature), 287.2K (0.5K warmer than pre-industrial), and 287.7K (1.0K warmer than pre-industrial). The upper two

brown lines represent two climate thresholds which have already been passed, as indicated by the two inset boxes. Within these two inset boxes, the y-axis represents probability (from 0 to 1) whereas the x-axis remains in years. The thick purple line within these inset boxes is the probability that the corresponding threshold was crossed by a given year. b) EBM-Kalman Filter and Temperature Forecast Thresholds: As in Fig. 3, there is the EBM-Kalman Filtered state estimate (navy blue line), a 2σ confidence interval of the innovation covariance (S_n) in light blue (around the a priori estimate). As in Fig. 4a, there are GMST measurements in gray dots, and 3 horizontal brown lines representing climate thresholds, the upper two at pre-industrial +0.5K and pre-industrial +1.0K. Within these two inset boxes, the y-axis represents probability (from 0 to 1) whereas the x-axis remains in years. The thick purple line within these inset boxes is the probability that the corresponding threshold was above a simulated draw from the a priori state.

Note that both threshold crossing probabilities in thick purple track with the EBM-Kalman Filtered state estimate in thin blue in Fig. 4b when aligned by year, although these two quantities are in entirely different probability domains. This results from both state and innovation covariances that remain stable during this window, together with the fact that the cumulative density function of the Gaussian distribution is roughly linear in the vicinity of the mean. As the EBM-Kalman Filtered state estimate approaches any given threshold, the cumulative temperature threshold approaches 0.5, or 50% at a "threshold crossing instant". The +0.5K threshold had crossing instants in 1989, 1991, and 1996, while the +1.0K threshold's crossing instant was in 2017. For the temperature forecast, the threshold crossing periods were 1981-1998 for +0.5K, and 2013-present for +1.0K. As mentioned above, the threshold crossing periods for the climate state were briefer: 1988-1996 for +0.5K and 2016-2018 for +1.0K (see Fig. 9).

4. Optional Refinements

a. Time-Varying Measurement Uncertainty and RT Smoother

This past-to-present Kalman Filter described in (5-13) can be extended into a RTS smoother (RTS) (Rauch, Tung et al. 1965) by additional steps (14-16), which encompass all known measurements into each estimated state by running backward from the last known estimates of $\hat{x}_n$ and P_n.

$$\hat{K}_n = P_n\Phi_n/P_{n|n-1} \qquad \text{back-updated Kalman gain} \qquad (14)$$

$$\hat{\hat{x}}_n = \hat{x}_n + \hat{K}_n\left(\hat{\hat{x}}_{\mathrm{n}} - F(\hat{x}_n;u_{n+1})\right) \qquad \text{back-updated state estimate} \qquad (15)$$

$$\hat{P}_n = P_n + (\hat{P}_{n+1} - P_{n|n-1})\hat{K}_n^2 \qquad \text{back-updated state covariance} \qquad (16)$$

This RTS has a theoretical advantage of blending abrupt changes in the model state over greater time periods, while also slightly reducing the state covariance. For instance, if the measurements suddenly and persistently diverged from the blind, forward EBM, an EBM-Kalman Filter model state would only react as these measurements diverge, whereas an EBM-RTS would foreshadow this jump. For the purposes of this paper, these distinctions make little difference, as is demonstrated in Fig. 5 below. Note that between 1850 and 1860 the intentionally overestimated initial state uncertainty P_0 of 1K is reduced through successive filtering steps in the EBM-Kalman Filter, and bi-directional smoothing steps within the EBM-RTS.

The uncertainty in the climate state P_n automatically responds to unexpected values of the measured temperature, which might occur if the weather variability in the climate increases. (Wunsch 2020) Regardless of whether this dynamic occurs, measurement uncertainty ought to reflect the improving global measurement system accuracy. Thus, an alternative modification of the original EBM-Kalman Filter incorporates the known uncertainty in the HadCRUT5 measurements of GMST, which decreases in standard deviation from 0.079K in the 1850-1879 window to 0.017K in the 1990-2019 window (see Figure 4 of HadCRUT5 (Morice, Kennedy et al. 2021)). This shrinking uncertainty primarily reflects a lack of observations in the Southern hemisphere before the satellite age. The total climate "emission" uncertainty can then be decomposed into two summed components: the physical measurement uncertainty in GMST, and the state-to-measurement uncertainty reflecting random-noise processes, sampling, and representativeness errors that make GMST estimates deviate from the underlying climate state. We assume the covariance between these two sources of uncertainty is 0 and simply sum the two variances to obtain a time-varying value of R_n (TVR). In Fig. 5 this causes the EKF-TVR state uncertainty $\sqrt{\breve{P}_n}$ to shrink from its initial value of 1K slightly more slowly than $\sqrt{P_n}$, because for many decades there is greater measurement uncertainty, so the filtering steps of this EKF-TVR cannot obtain as much information from the early GMST measurements to constrain the uncertainty.

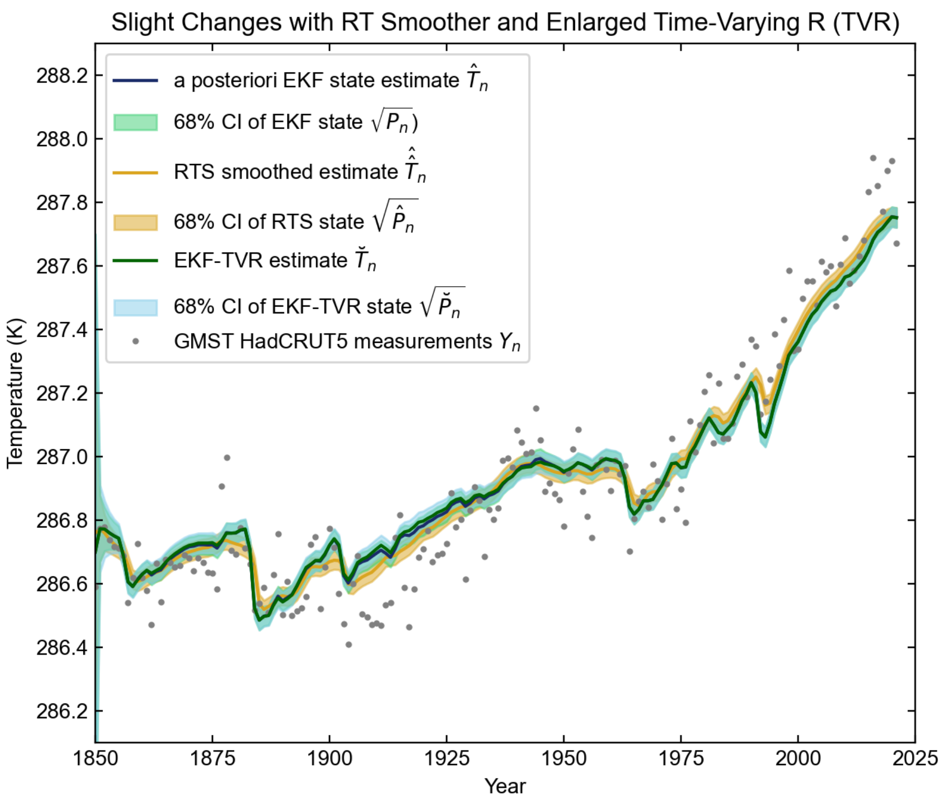

Fig. 5: Comparisons of the original EBM-Kalman Filtered climate state (navy blue line with green 1σ uncertainty window) with an EBM-RTS climate state (red line with red 1σ uncertainty window) and the effects of incorporating additional time-varying measurement uncertainty (green line with light blue 1σ uncertainty window). The addition of extra time-varying measurement uncertainty makes very little difference to the EBM-Kalman Filtered climate state, except from 1905-1930 when it lessens the deflection of repeated cooler GMST temperature measurements. In contrast, the EBM-RTS climate state doubly takes these annual temperature measurements into account, so it has a greater cooling deflection in this period, and many years that are warmer than the EBM-Kalman Filtered climate state after 1980, although even these differences are slight - at most 0.1K during years of volcanic activity.

b. Non-Gaussian Future Projection and Sampling of Volcanic Activity

Any EBM-Kalman Filter can project into the future without any new measurements. This simply involves repetitively using just equations 2.2 and 2.3, and then taking the a posteriori state and a posteriori covariance to be the a priori (projected) state and a priori covariance: $\hat{\mathbf{x}}_{\mathbf{n}}=\mathbf{F}(\hat{\mathbf{x}}_{\mathbf{n-1}})$ and $P_n=\Phi_n^2 P_{n-1}+Q$. While this means that the state covariance is linearly growing, here Q is very small (variance ~ 0.00037), and so over a 79-year future projection (2022-2100) the state covariance only grows from a 1σ uncertainty of 0.0307K to between 0.0352K and 0.0355K, a 16% increase that is imperceptible over this century (Fig. 6).

A slightly more complex issue regarding future projections is generating the two time series inputs into the blind EBM, namely the concentrations of greenhouse gasses including carbon dioxide ($[CO_2]_n$) and stratospheric aerosols due to volcanic dust (AOD_n). Future carbon dioxide concentrations are given by representative concentration pathways (RCPs), which numbered according to the projected CO_2 radiative forcing in 2100 relative to the preindustrial climate (https://tntcat.iiasa.ac.at/RcpDb/). For instance, we picked RCP2.5 and RCP6.0 in Fig. 6, which flank the most likely result of current environmental policies. (Pielke Jr, Burgess et al. 2022). Volcanic eruptions determining AOD_n are inherently stochastic, but the time intervals between eruptions can be approximated using exponential distributions (Papale 2018). No single exponential distribution fits well to the observed series of time intervals, so an exponential mixture with two components was found to be the best fit to the data using the decomposed normalized maximum likelihood. (Okada, Yamanishi et al. 2020) See Appendix C for further details.

While these distribution approximations may be imperfect from the perspective of a volcanologist, for our purposes they simply allow reasonable-looking samples of future aerosol optical depths to be fed into the EBM-Kalman Filter. Even though the EBM-Kalman Filter is built on the assumption of Gaussian error, it is so computationally simple that it can be used to sample complex non-Gaussian distributions.

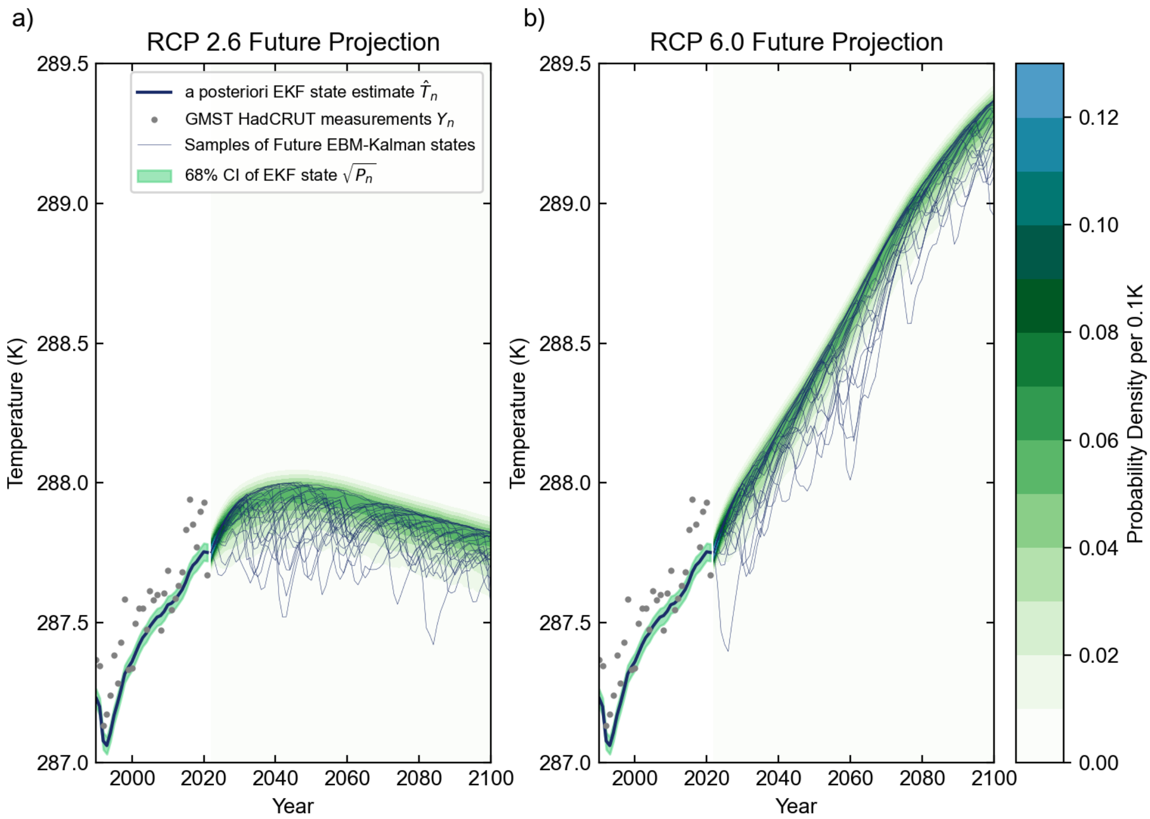

Fig. 6: Future projections of RCP2.6 (6a) and RCP6.0 (6b) scenarios using sampled measures of volcanic activity. RCP2.6 in Fig 6A is a very stringent future scenario in which CO_2 emissions sharply decline after 2020 to keep GMST rise below 2°C (van Vuuren, den Elzen et al. 2007). RCP6.0 in Fig 6B is a much higher emission scenario in which CO_2 emissions do not peak until 2080 (Fujino, Nair et al. 2006; Hijioka, Matsuoka et al. 2008). The median estimate based on current environmental policies projects warming of 2.2°C to reach a GMST of 288.9K by 2100. (Pielke Jr, Burgess et al. 2022). The historical Mt. Pinatubo eruption in 1991 is shown in the lower left corner of both graphs for scale. 25 of the sampled 500 potential future climate states are graphed as thin navy-blue lines. The probability density function formed by taking the summation of all sampled gaussian kernels at each time point is shaded in green. Note that this probability density is not symmetrical - there is a much more gradual tapering off on the cooler side because of volcanic eruptions. Indeed, the volcanic eruptions dominate the future uncertainty over the slowly growing state uncertainty. There is a gap from 2021 to 2022 between the past EKF state estimates and future projections, to emphasize the distinction between these even though the same state estimate and state covariance is carried forward in time for each future sample.

5. Discussion

a. Comparison to a Large Coupled Model - CESM2

The EBM-Kalman Filter framework is chiefly advantageous because it replicates the major statistical features of an ensemble of large coupled climate models, while being trivial to compute. Therefore, we analyze the statistical features of one such ensemble, particularly the 90 runs of LENS2 (Rodgers, Lee et al. 2021). The distribution of annual differences of all model trajectories from the ensemble mean are remarkably close to Gaussian. (Fig. 7) Therefore, this fundamental assumption of the EBM-Kalman Filter is also met by the CESM2 large coupled climate model. While the standard deviation does rise with time in this large ensemble ($p=0.002$) indicating increasing internal variability with climate change, this effect was relatively small ($r^2=0.105$ and the rise was only 9.4% from 1850-2050). The time-averaged standard deviation of 0.127K was close to both the chosen value of $\sqrt{(R)} = 0.105$K and to the converged value in the EBM-Kalman Filter of the innovation covariance $\sqrt{S_n} =$ 0.110K.

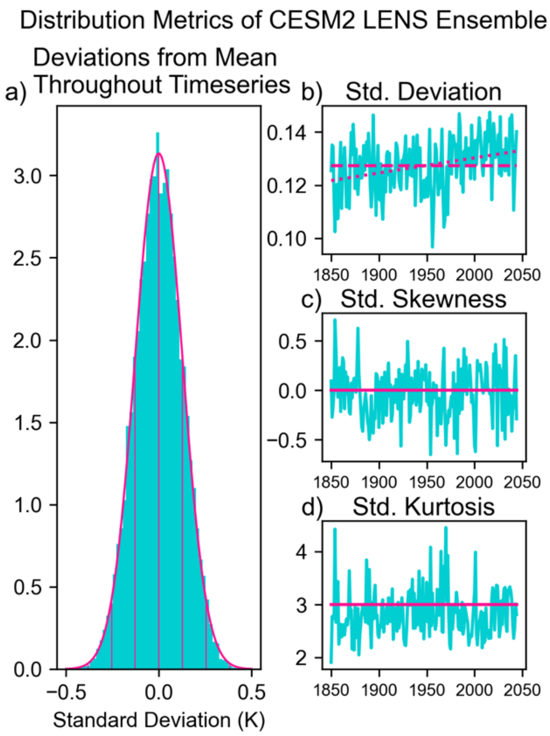

Fig. 7: Statistical Features of the CESM2 Large Ensemble. (Rodgers, Lee et al. 2021). Pink lines in the histogram in (7a) depict an ideal Gaussian distribution with standard deviation of 0.126K, and vertical lines drawn for each of these standard deviations. Solid pink lines for the skewness and kurtosis indicate the ideal values for a Gaussian distribution. The observed trend in the standard deviation over time is plotted in a dotted pink line in the top-right corner.

Next, we evaluated how well this LENS2 captures the overall shape of the observed HadCRUT5 temperatures, given that it is not constrained directly by these observations. We wish to draw attention to the fact that in order to create this figure, the absolute temperature of the LENS2 runs had to be revised down by a full 1.75K to match the 1960-1990 30-year climate normal (Jones and Harpham 2013). Other authors have also noted this high absolute temperature as well as the high climate sensitivity of CESM2. (Gettelman, Hannay et al. 2019; Feng, Otto-Bliesner et al. 2020; Zhu, Otto-Bliesner et al. 2022)

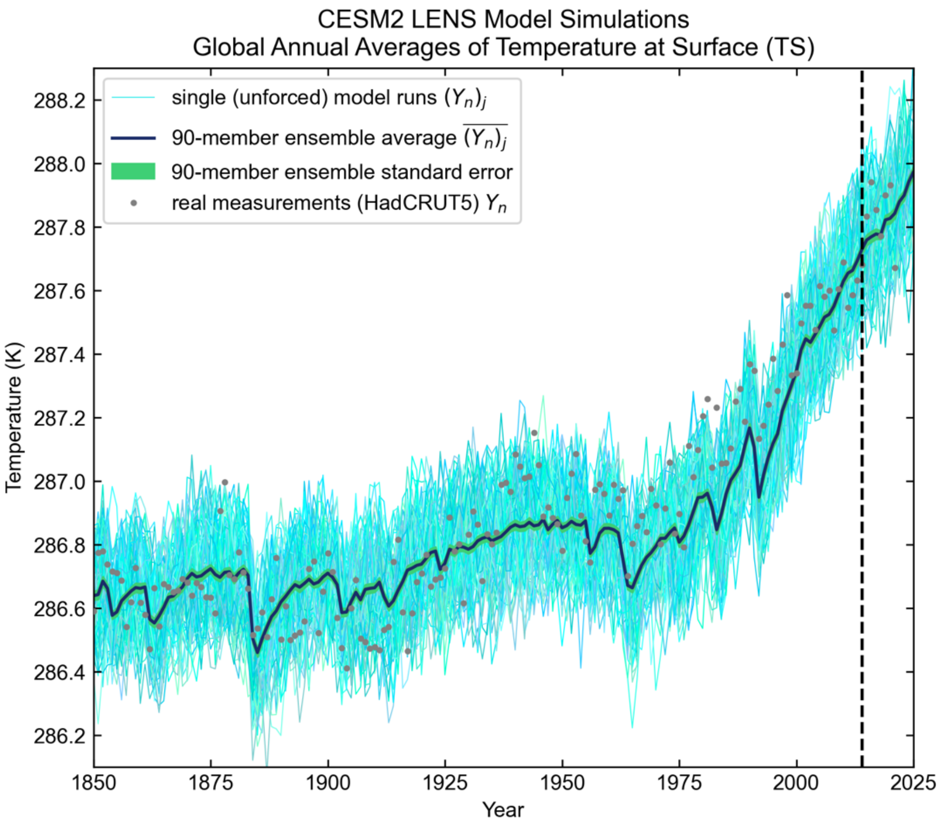

Fig. 8: Comparison of the CESM2 Large Ensemble (LENS2). (Rodgers, Lee et al. 2021) with HadCRUT5 measurements. The various shades of thin light blue and turquoise lines represent each individual simulation $(Y_n)_j$ of the 90-member ensemble. The ensemble mean is plotted in a navy-blue line, and the ensemble standard error is plotted around this line in green. This standard error in green is the standard deviation divided by the square root of the number of runs in the ensemble at that moment and shows the 1σ uncertainty in the yearly simulated climate is roughly 0.013K. Also, the ensemble mean has $r^2 = 0.83$ relative to the HadCRUT5 measurements, slightly lower than for the blind EBM. The dashed vertical line represents future simulations at the time of the construction of LENS2.

Regarding the various types of climate thresholds, the LENS2 can be used to generate very similar results to the EBM-Kalman Filter. Differences in absolute probability and threshold crossing instants reflect differences in the modeled climate states: particularly that the CESM2 was cooler than the energy-balance model in the 1980s and 1990s, whereas the opposite was the case after 2000 (Fig. 9).

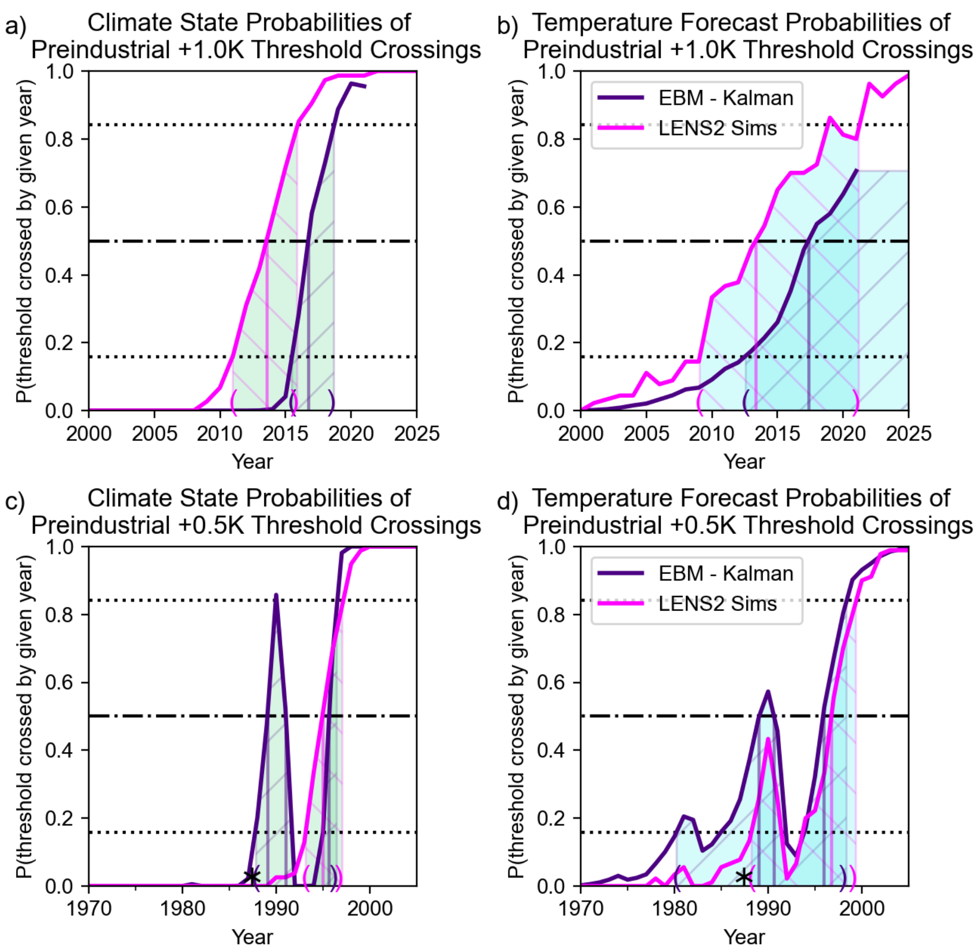

Fig. 9: Comparison of Historical Threshold Crossing Probabilities for the EBM-Kalman Filter (dark purple) and CESM2 LENS simulations (pink). Note that the dark purple lines are the same as those graphed in the inset axes within Figure 4. The left panels (a and c) display probabilities relevant to climate states with 21-year averages of the CESM2 simulations, whereas the right panels (b and d) display the temperature forecasts. Top panels (a and b) display the preindustrial +1.0K threshold, whereas the bottom panels (c and d) display the earlier preindustrial +0.5K threshold. Additionally, the threshold crossing instants are marked with thick vertical lines within all panels. The threshold crossing windows are lightly shaded and hashed: with light blue shading for temperature forecast windows, light green shading for climate state windows, positively sloping hashing in dark purple for the EBM-Kalman Filter, and negatively sloping hashing in pink for LENS2. The cross-hatched regions indicate where the EBM-Kalman Filter and LENS2 agree regarding the threshold crossing windows. The limits of these crossing windows are also drawn with parentheses on the time axis in dark purple for the EMB-Kalman filter and pink for LENS2. A black asterisk indicates 1987, the year that 30-year running mean of GMST crossed the +0.5K threshold in the bottom panels (c and d), whereas the latest 30-year mean centered in 2007 is below the +1.0K threshold.

We also compared future EBM-Kalman Filter projections with LENS2 projections. Both graphs trace out roughly the same shapes, although the SSP370 experiment portion of the LENS follows RCP7.0, which had more intense forcing than what was projected in RCP6.0 (see Figure 6B). Also, the largely symmetric variation in the large coupled model is driven by dynamical instability. This is fundamentally different from the EBM-Kalman Filter, which samples a noisy distribution of volcanic eruptions, yielding asymmetrical variation. This illustrates a major advantage of this system: thousands of future scenario inputs can be generated and utilized within seconds on a mere personal computer (see Fig. 6). In contrast, each of the LENS2 simulations took over a week to run on part of a supercomputer cluster ($>10^{10.5}$ times slower) and gave every simulation an identical projection of volcanic activity: an aerosol optical depth prescribed to a fixed annual cycle depending on latitude and altitude.

b. Sampling from a member - need to enlarge the model uncertainty for ensemble spread

There are many more past and future climate scenarios that researchers wish to investigate than there are computational resources to run a full large coupled ensemble for each scenario. Fortunately, the EBM-Kalman Filter allows for one or a handful of large coupled climate model simulations to approximate the distribution of an entire ensemble spread (similar to an approach taken for ensembles of ice sheet models in (Edwards, Nowicki et al. 2021)). The average “climate state uncertainty” $\sqrt{P_n}$ following one model ensemble member (~0.038K) nearly covers the spread of “climate states” $(\hat{T}_n)_j$ within the entire LENS2 simulation ensemble (Fig 10a,e), which relative to each other are distributed with a standard deviation that is only 1.32 times larger. So the EBM-Kalman Filter approximates what “state uncertainty” intuitively means within the context of a large coupled ensemble, a result especially remarkable because the error terms (R and Q) were based on the HadCRUT5 dataset alone, not LENS2. HadCRUT5 measurements themselves can also roughly approximate the LENS2 “state uncertainty” (see Fig. 10a,b,c). However, there are inter-annual differences which persist between runs of the ensemble and skew some climate states $(\hat{T}_n)_j$ cooler and others warmer (Fig. 10d). Also, it is unknown if the current generation of large coupled climate models have the ability to represent the full spread of climate states appropriately. For instance, weather models use stochastic variation to push their distribution wider than dynamic variation alone (Buizza, Milleer et al. 1999), and the IPCC interprets the 2-sigma ensemble spread as the probability range associated with only a 1-sigma spread ((Lee, Marotzke et al. 2021), Box 4.1). Therefore, we empirically recommend doubling $\sqrt{P_n}$ to cover a distribution of unknown “climate states” based on a single simulation.

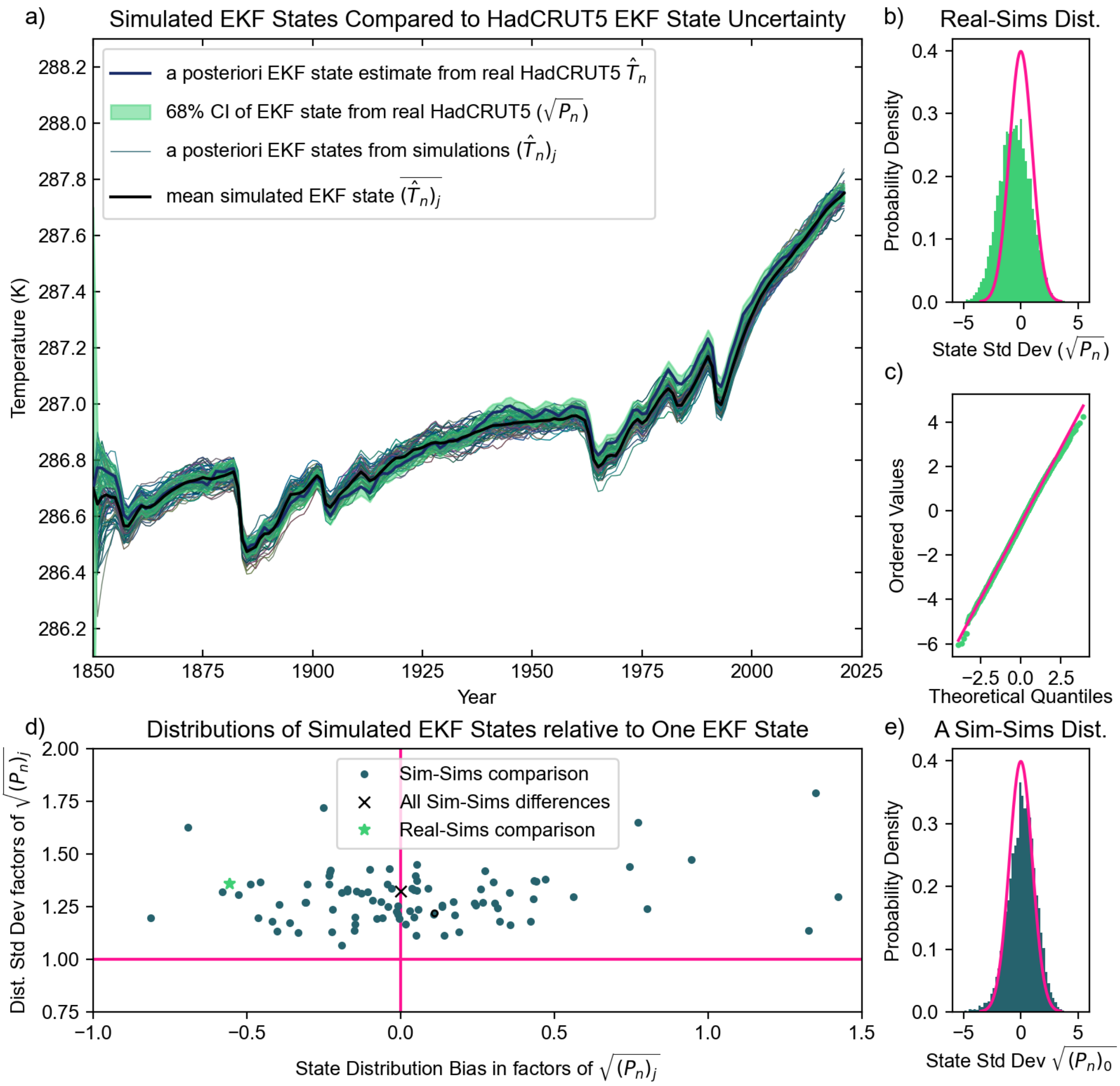

Fig. 10: Comparison of the Kalman Filter States across the LENS2 ensemble. a) The mean Kalman Filtered state estimate (thick black line) is drawn with all individual Kalman Filtered state estimates assimilating individual CESM2 simulations (rather than measurements of real GMST) also drawn as blue-gray lines. A 1σ state confidence interval is shown around the HadCRUT5 measured GMST's Kalman Filtered climate state (light green area). b) The differences between the "real" measurement based HadCRUT5 climate state and all LENS2 climate states, scaled by the state standard deviation and plotted against the ideal normal distribution. The empirical and ideal distributions approximately match, demonstrating that even without adjustment the majority of LENS2 climate states are within the climate state uncertainty window assumed by the original HadCRUT5-based EBM-Kalman Filter. c) In the qqnorm plot, these differences between the "real" measurement based HadCRUT5 climate state and all LENS2 climate states nearly follow a straight line. d) Climate states and associated uncertainties arising from each of 89 LENS2 simulations and HadCRUT5 are compared to all other LENS2 climate states, and the bias and standard deviation of the resulting empirical distributions are plotted. One LENS2 simulation had early missing data, preventing the EBM-Kalman from running on it. e) One of these empirical distributions is graphed, indicated by the point circled in black within the scatterplot.

c. Future Extensions

We emphasize that this first iteration of a climate Kalman filter does not generate regional temperatures nor other essential climate variables, such as precipitation. It also does not capture regional "tipping points" or other important nonlinear process aspects of climate change. Therefore, this first climate Kalman filter is far from generating the information required to compare it to large ensembles. However, we also note that this Kalman framework was designed to be utilized on a vector of state parameters, and we are only currently utilizing scalar values of GMST. Other terms in a potential global climate state vector, such as precipitation, seasonal temperature, or eigenvalues of spatially decomposed principal components of the climate system (for instance the El Nino / Southern Oscillation) could be appended into this Kalman framework with appropriate simple physical forward modeling. (Yang, Li et al. 2018)

Additionally, we experimented with Bayesian parameter search to give better estimates of the coefficients in the blind energy-balance equation. The prior distributions of these coefficients can be extracted from climate science literature, followed by a Metropolis-Hastings search. However, identifiability and overfitting remain challenging and deserve more attention than the scope of this introduction allows. Several parameters must be tuned proportionally for certain constraints to be maintained (particularly no net energy transfer in the preindustrial climate), such as the main coefficient multiplying all longwave radiation terms and the power on the temperature (currently 2.385 in the original energy-balance model). Astute readers may observe that the most recent years of the blind energy-balance model (and thus the Kalman filtered state) appear cooler than both the Hadcrut5 and the CESM2 LENS predictions. We decided to use all point estimates given by literature sources rather than tuning any feedback to avoid unnecessary complexity. But this issue of underestimating the recent climate may be most directly fixed by increasing the CO_2 feedback to a greater W/m^2 of energy absorbed per order of magnitude of CO_2 increase (see Eq. A15). This change would represent a larger forcing due to anthropogenic atmosphere changes that scale with CO_2, or reduced reflective aerosol feedbacks to offset these forcings (see Fig 7.6 of Forster et al. 2021).

Finally, the Kalman filtering framework may be utilized in process control (Myers and Luecke 1991; Lee and Ricker 1994) to optimize various climate change mitigation strategies (Filar, Gaertner et al. 1996; MacMartin, Kravitz et al. 2014; Kravitz, MacMartin et al. 2016).

6. Conclusion

The EBM-Kalman Filter presented in this paper represents somewhat of a compromise between a 30-year running average of GMST (the historical definition of climate) and the state-of-the-art large coupled climate model ensembles such as CESM2 LENS. The variance of the EBM-Kalman Filtered climate state is easily constructed to be very close to that of a running 30-year mean, and this filtered climate state then does an excellent job in describing the overall shape of the measured temperature values ($R^2 = 0.88$). However, this EBM-Kalman Filter has no lag: as soon as measured values are reported for the current year, it can describe the climate state, unlike the 30-year mean which can only describe what the climate was 15 years ago. In comparison to the ensemble spread of an ensemble of coupled climate models, which is presently the typical brute-force method for quantifying internal variability, there is a very similar Gaussian statistical distribution. In contrast the EBM-Kalman Filter approach has very transparent, clean physical parameters that can be directly measured (or taken from estimates in literature) leading to trivial uncertainty quantification. The computational cost of the EBM-Kalman Filter is negligible, so future predictions can sample from probability distributions approximating intermittent volcanism, unlike coupled climate models. This EBM-Kalman Filter framework can additionally be used to easily calculate various definitions of climate thresholds, which have significant policy implications. While it does not predict all climate variables of interest, it is a powerful, transparent, and inexpensive tool that may be readily combined with other approaches.

Acknowledgments.

JMN, BFK, and CL were funded by ONR N00014-17-1-2393. Conversations with Jochem Marotzke and Lorraine E. Lisiecki helped to focus this work.

Data Availability Statement.

This study performed re-analysis of existing datasets openly available at locations provided in Appendix A, in Section 4b, or for LENS2 and HadCRUT5 at https://www.earthsystemgrid.org/dataset/ucar.cgd.cesm2le.atm.proc.monthly_ave.TS.html and https://www.metoffice.gov.uk/hadobs/hadcrut5/data/current/download.html respectively. Further documentation about data processing including Python code is available at the Brown Digital Repository at [*insert DOI here]*.

APPENDICES

Appendix A: *Derivation of the Blind Energy-Balance Model*

Units are omitted in this section within equations for clarity of the mathematical derivation, but they are retained within the text and reincorporated in A32 and A24.

$$\Delta\text{Energy} = \phi_{SW}(\text{in}) - \phi_{LW}(\text{out}) \tag{A1}$$

$$\frac{T_{n+1}-T_n}{k} C_{heat} = G_0 * \tilde{d}_n * f_{\alpha A}(T_n) * f_{\alpha S}(T_n) - j^{\star} * \tilde{g}_n * f_{H2O}(T_n) \tag{A2}$$

k is 1 year, the time step of this iterative model. n represents the calendar year (e.g. 2000). On the right side of the equation, both the shortwave radiative flux and longwave radiative flux take the same form: (source) * (prescribed attenuation) * (feedback attenuation). C_{heat}, the heat capacity of the climate system, was known imprecisely: 17 ± 7 W (year) m^{-2} K^{-1}, (Schwartz 2007), however this heat capacity value has a relatively minor impact on the overall model performance.

G_0 is the extraterrestrial irradiance, taken to be (solar irradiance)/4 =1360 W/m^2 / 4 = 340 W/m^2. While the annual extraterrestrial irradiance varies by 0.1% between solar minima and solar maxima on a cycle lasting about 11 years (Willson and Hudson 1991; Wang, Lean et al. 2005; Kopp and Lean 2011), within this model it was assumed a constant.

$\tilde{d}_n$ is the prescribed shortwave light attenuation due to volcanic dust. This stochastically varying quantity can be calculated from the stratospheric optical depth AOD_n (Sato, Hansen et al. 1993; Vernier, Thomason et al. 2011) according to the formula given by Harshvardan and King (1993; Schwartz, Harshvardhan et al. 2002). (g=0.853 is the middle of the given range). The AOD_n values used are forcings for the GISS climate model from 1850 - 1978 (https://data.giss.nasa.gov/modelforce/strataer/tau.line_2012.12.txt, AOD_n at 550nm) and globally averaged measurements from the GloSSAC_V2 satellite measurement product (Nasa/Larc/Sd/Asdc 2018) from 1979 – 2021 (https://asdc.larc.nasa.gov/project/GloSSAC/GloSSAC_2.0, AOD_n at 525nm).

$$\tilde{d}_n = \frac{1.33}{AOD_n*(1-g)+1.43}, \quad g \in [0.834, 0.872] \tag{A3}$$

$$\tilde{d}_n \approx \frac{9.07}{AOD_n+9.73} \tag{A4}$$

$f_{\alpha A}(T_n)$ is the additional atmospheric shortwave attenuation due to cloud albedo, while $f_{\alpha S}(T_n)$ is the surface shortwave attenuation due to ground albedo. Taken together, these two terms yield an overall absorption of 0.707 as measured by the measured from March 2000 to February 2005 by the CERES satellite (Wielicki, Barkstrom et al. 1996; Loeb, Wielicki et al. 2009), or equivalently a top-of-atmosphere, all-sky albedo of 0.293. Decomposition of this overall albedo into its clear-sky component (0.153) yields a ground absorption fraction of 0.847. Noting the small volcanic dust in the atmosphere during this time frame, the total shortwave attenuation can be used to solve for both components:

$$0.707 \approx \tilde{d}_n * f_{\alpha A}(T_n) * f_{\alpha S}(T_n) \approx \frac{9.07}{0.002+9.73} * f_{\alpha A}(T_n) * 0.847 \tag{A5}$$

$$0.896 \approx f_{\alpha A}(T_n), \quad \text{for} \quad n \in [2000,2005] \tag{A6}$$

$j^\star = \sigma_{sf} T_n^4$ is the ideal black body radiation or Planck feedback, which derives from quantum mechanics, particularly the Stefan-Boltzmann law (Boltzmann 1884), which gives the Stefan-Boltzman constant $\sigma_{sf} = 5.670\ 10^{-8} Wm^2K^{-4}$ as a coefficient. For the Earth, because the temperature is in the neighborhood of 287K, this black body radiation is primarily in the infrared spectrum, between 200 and 1200 cm^{-1} (Zhong and Haigh 2013).

$\tilde{g}_n$ is the prescribed longwave attenuation due to CO_2, which is half of the fraction of radiative energy absorbed by those CO_2 (because half is re-emitted upwards and half downwards). This absorbed, downwards-emitted fraction is directly proportional by β_0 to the logarithm of the CO_2 concentration (see Figure 6b of (Zhong and Haigh 2013)). CO_2 concentrations were taken as the historical concentrations used in the NASA GISS climate model 1850-1979 (https://data.giss.nasa.gov/modelforce/ghgases/Fig1A.ext.txt) and the NOAA global averages from 1980-2021 (https://gml.noaa.gov/webdata/ccgg/trends/co2/co2_annmean_gl.txt).

$$\tilde{g}_n = \frac{E_{absorbed}}{2j^\star} \approx \beta_0 + \beta_1 \log_{10}([CO_2]_n) \tag{A7}$$

$f_{H2O}(T_n)$ is the additional atmospheric longwave attenuation due to water vapor and other gasses, including both lapse rate and relative humidity. The precise functional form of this feedback function is unknown, as is the functional form of the two shortwave feedbacks, partially due to disagreements between paleoclimate inferences and globally coupled climate models. We thus introduced the following 3 functions, which incorporate an additional 3 positive β coefficients and 1 exponent. (Note p_0=4, the exponent on the $j^\star$ term.)

$$f_{H2O}(T_n) \doteq (1/T_n)^{p_1} \tag{A8}$$

$$f_{\alpha A}(T_n) \doteq 0.896\left(1+\beta_2 (T_n - T_{2002})^{p_2}\right) \tag{A9}$$

$$f_{\alpha S}(T_n) \doteq 0.847\left(1+\beta_3 (T_n - T_{2002})^{p_3}\right) \tag{A10}$$

Now, following the definition of climate sensitivity of z as ∂*N*/∂w * dw/dT, where *N* is the TOA radiative flux (the entire right side of the model), we expressed the climate sensitivity of each of the three *f* feedback functions and the Planck response $j^\star$, as reported in Table 7.10 and Figure 7.10 of AR6 (Forster, Storelvmo et al. 2021).

$$\frac{\partial N}{\partial j^\star} * \frac{d\, j^\star}{dT_n} = -\tilde{g}_n * f_{H2O}(T_n) * 4\sigma_{sf}(T_n)^3 = -3.22 \tag{A11}$$

$$\frac{\partial N}{\partial f_{H2O}(T_n)} * \frac{d\, f_{H20}(T_n)}{dT_n} = -j^\star * \tilde{g}_n * -p_1(T_n)^{-p_1-1} = 1.30 \tag{A12}$$

$$\frac{\partial N}{\partial f_{\alpha A}(T_n)} * \frac{d\, f_{\alpha A}(T_n)}{dT_n} = 340 * \tilde{d}_n * f_{\alpha S}(T_n) * 0.896\beta_2 = 0.35 \tag{A13}$$

$$\frac{\partial N}{\partial f_{\alpha S}(T_n)} * \frac{d\, f_{\alpha S}(T_n)}{dT_n} = 340 * \tilde{d}_n * f_{\alpha A}(T_n) * 0.847\beta_3 \approx 0.42 \tag{A14}$$

Solving for the exponent by taking the ratio of the first two equations yielded $p_1=1.615$. Furthermore, based on the CERES measurements from 2000-2005, everything to the left of both β_2 (A13) and β_3 (A14) is the overall absorbed SW radiance of 340*0.707=240.5 W/m^2, so $\beta_2 = 0.00146$ K^{-1} and $\beta_3 = 0.00175$ K^{-1}.

Figure 3.3 from Zhong and Haigh (2013) shows that per order of magnitude of [CO2] increase, an additional 15.45 W/m^2 is absorbed. Because there are additional anthropogenic greenhouse gasses such as methane, the net contribution is slightly higher than this, by a fraction of 2.72 W/m^2 / 2.16 W/m^2, so assuming CO_2 remains the same proportion to these other gasses, an additional 19.45 W/m^2 is absorbed per unit of $\log_{10}$ [CO2] increase. (see AR6 (Forster, Storelvmo et al. 2021), Figure 7.6 and Table 7.8) This measurement approximating a partial derivative was presumably made recently, so we used the more recent 2002 temperature of ~287.5K (14.4°C), but this choice is relatively inconsequential: $\beta_0\beta_1$ would be only 0.66% larger if the pre-industrial temperature were used instead. In the pre-industrial climate, we assumed a steady-state equilibrium with a constant black body temperature of 286.7K (13.6°C) and a log10([CO2]) ≈ 2.45. This allows us to solve for β_0 and β_1 as follows:

$$19.45 = \frac{\partial N}{\partial f_{H2O}(T_n)} * \frac{d\, f_{H20}(T_n)}{d\ \log_{10}([CO_2]_n)} = -\sigma_{sf}(T_n)^4\beta_1(T_n)^{-1.61}\left(-\beta_0\right) \tag{A15}$$

$$456.4 = \beta_1\beta_0 \quad \text{using} \quad T_{2002}=287.5 \tag{A16}$$

$$0 = 340\tilde{d}_n * f_{\alpha A}(T_{1850}) * f_{\alpha S}(T_{1850}) - \sigma_{sf}(T_{1850})^4\beta_1(T_{1850})^{-1.61}\left(1-\beta_0(2.45)\right) \tag{A17}$$

$$241.1 = \sigma_{sf}(286.7)^{2.39}(\beta_1)\left(1-\beta_0(2.45)\right) \tag{A18}$$

$$5656 = (\beta_1)\left(1-\beta_0(2.45)\right) \tag{A19}$$

$$6972 \approx \beta_1 \quad \text{and} \quad 0.0655 \approx \beta_0 \tag{A20}$$

Checking that Planck partial derivative is accurate, we obtained a value for climate sensitivity of $j^\star$ to be -3.34 $W/m^2/K$ at current conditions and the sensitivity of f_{H2O} to be 1.35 $W/m^2/K$, well within the likely range of AR6. However, with an instantaneous doubling or quadrupling of CO_2 the sensitivity of $j^\star$ becoems-3.30 $W/m^2/K$ or -3.22 $W/m^2/K$ respectively. Because they were defined to have proportional climate sensitivities, f_{H2O} exactly matches AR6 in a 4xCO_2 scenario, with 1.30 $W/m^2/K$.

This yielded a blind energy-balance model with good skill at predicting the GMST (orange dashed line in Fig. 2), $r^2 = 0.88$. Reducing and differentiating:

$$T_{n+1} = T_n + 137.65\frac{\left(1+0.00146(T_n\text{-}287.5)\right)\left(1+0.00175(T_n\text{-}287.5)\right)}{AOD_n+9.73}$$

$$-0.00002325(T_n)^{2.39}\left(1\text{-}0.0655\log_{10}([CO_2]_n)\right) \tag{A21}$$

$$\frac{\partial T_{n+1}}{\partial T_n} = 1+\frac{0.441}{AOD_n+9.73}\left(1+0.00159(T_n\text{-}287.5)\right)$$

$$-0.00005546(T_n)^{1.39}\left(1\text{-}0.0655\log_{10}([CO_2]_n)\right) \tag{A22}$$

Further simplifying to nondimensionalize all units:

$$T_{n+1} \quad = \quad T_n+\frac{137.7\text{m}}{AOD_n+9.73\text{m}}\left(1+\frac{T_n\text{-}287.5\text{K}}{687.1\text{K}}\right)\left(1+\frac{T_n\text{-}287.5\text{K}}{572.6\text{K}}\right)$$

$$-\left(\frac{T_n}{274.9\text{K}}\right)^{2.385}\log_{10}\left(\frac{1.893*10^{15}\text{ppm}}{[CO_2]_n}\right) \quad = \quad F(T_n;[CO_2]_n,AOD_n) \tag{A23}$$

$$\frac{\partial T_{n+1}}{\partial T_n} \quad = \quad 1+\frac{0.4407\text{m}}{AOD_n+9.73\text{m}}\left(1+\frac{T_n\text{-}287.5\text{K}}{629.9\text{K}}\right)$$

$$-\left(\frac{T_n}{8464.\text{K}}\right)^{1.385}\log_{10}\left(\frac{1.893*10^{15}\text{ppm}}{[CO_2]_n}\right) \quad = \quad \frac{\partial F(T_n;[CO_2]_n,AOD_n)}{\partial T_n} \tag{A24}$$

Appendix B: *Justification that the EKF is sufficient, will not diverge*

The issue of nonlinearity arises not in the computation of $\hat{x}_{n|n-1}=F(\hat{x}_{n-1})$ but rather the covariance distribution P_n of points (infinitesimal probability masses) neighboring $\hat{x}_{n-1}$, which are assumed to scale linearly around this transformation to maintain a normal distribution. Nonlinear distortion may pile more probability density onto a state other than the transformed original projection $F(\hat{x}_{n-1})$, necessitating a new computation of $\hat{x}_{n|n-1}$ as the mean of this distorted PDF. Thus, for an arbitrary point that is *z* standard deviations away from $\hat{x}_{n-1}$, the remainder error R_1 (Lagrange mean-value form) induced in a single cycle is:

$$F\left(\hat{x}_{n-1}+z\sqrt{P_n};u_n\right) - F(\hat{x}_{n-1}) - \frac{\partial F(x;u_n)}{\partial x} z\sqrt{P_n} =$$

$$R_1\left(\hat{x}_{n-1}+z\sqrt{P_n}\right)=\frac{\partial^2 F(\xi_L;u_n)}{\partial \xi_L^2}\frac{\left(z\sqrt{P_n}\right)^2}{2} \quad \text{for} \quad \xi_L \in \left[\hat{x}_{n-1}-|z|\sqrt{P_n}, \hat{x}_{n-1}+|z|\sqrt{P_n}\right] \tag{B1}$$

$$=\left(\frac{0.4407\text{m}}{\text{AOD}_\text{n}+9.73\text{m}}\left(\frac{1}{629.9}\right)-\left(\frac{1.385}{8464}\right)\log_{10}\left(\frac{1.893*10^{15}\text{ppm}}{[CO_2]_\text{n}}\right)\left(\frac{\xi_L}{8464.\text{K}}\right)^{0.385}\right)\frac{z^2 P_n}{2} \tag{B2}$$

$$-0.000284z^2P_n<R_1\left(\hat{x}_{n-1}+z\sqrt{P_n}\right)<-0.000246z^2P_n \tag{B3}$$

$$\frac{\left|R_1\left(\hat{x}_{n-1}+z\sqrt{P_n}\right)\right|}{|z|\sqrt{P_n}}<0.000284|z|*(0.0307)<|z|*10^{-5} \tag{B4}$$

This means that even if the error accumulates in the same direction in each cycle of the EKF, over the 171 year timeseries all probability masses that are within $|z|< 5.85$ standard deviations will have an error of <1%, compared to a particle method such as the Unscented Kalman Filter. (Julier and Uhlmann 1997; Wan and Van Der Merwe 2000)

Appendix C: *Generation of Volcanic Eruption Samplings*

As can be appreciated in Fig. C1a, long periods of no major volcanic eruptions (for instance 1935-1960) alternated with periods of many eruptions occurring in rapid succession (1883-1914, 1960-1994). Perhaps this observed pattern has some relation to magma or tectonic dynamics, but it prevented one Poisson distribution from describing the data well.

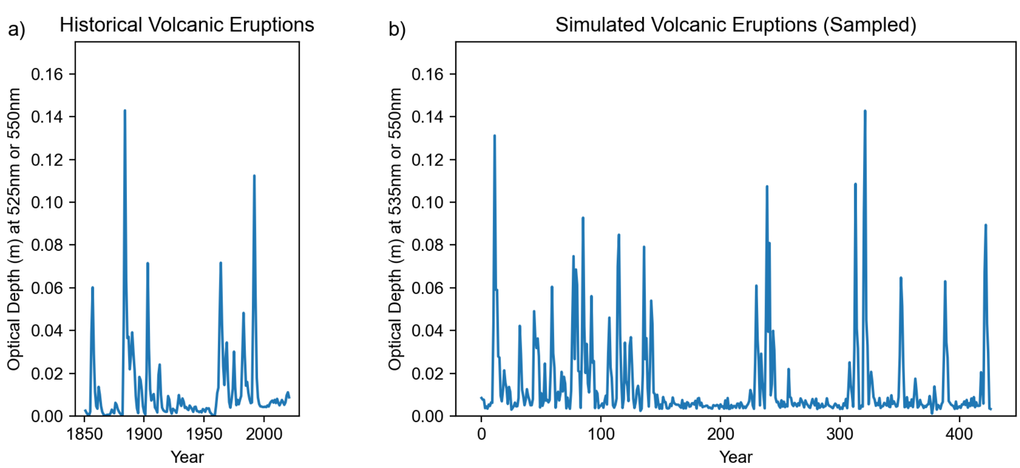

Fig. C1: Comparison of Historical Volcanic Eruptions (C1a) with Simulated Volcanic Eruptions (C1b), generated from a combination of several probability distributions.

Eruptions that occurred within 3 years were indistinguishable in the historical dataset, so the minimum time interval between simulated volcanic eruptions was 2.6 years plus a sample (Table C1) from the exponential mixture model i_n (Okada, Yamanishi et al. 2020). These intervals were rounded to integers. Similarly, the size of each volcanic eruption h_n was approximated using another shifted exponential distribution. The preceding year and two years following the eruption peak were positive fractions of the maximum aerosol optical depth, with gaussian blur. Similarly, non-volcanic years were positive gaussian noise (Table C2). Fig. C1b shows a sample from this combined generating function.

Exponential Distribution	Random Var.	Scale (units)	P(choose) (if mixture)
Interval Between: round($i_{n,0}$ + 2.6)	$i_{n,0}$ ~ Exp	2.263 (years)	88.9%
Interval Between: round($i_{n,1}$ + 2.6)	$i_{n,0}$ ~ Exp	24.2 (years)	11.1%
Peak Size: $AOD_n = h_n + 0.0082$	h_n ~ Exp	0.0339 (m)	

Table C1. Exponential Parameters of Volcano Generating Function. This generating function starts with a list of zero values for all AOD_n, and first samples several of these n years to be major volcanic eruptions. “Interval Between” refers to the interval in years between two successive major volcanic eruptions.

Gaussian Distribution	Random Var.	Mean μ (units)	Std Dev σ
Pre-Peak: $AOD_{n-1} = a_{-1} * E_n$	a_{-1} ~ Norm>0	0.51	0.25
Post-Peak 1: $AOD_{n+1} = a_1 * E_n$	a_1 ~ Norm >0	0.61	0.16
Post-Peak 2: $AOD_{n+2} = a_2 * E_n$	a_2 ~ Norm >0	0.32	0.16
Other Years: $AOD_n = a_0$	a_0 ~ Norm >0	0.00371 (m)	0.00286 (m)

Table C2. Gaussian Parameters of Volcano Generating Function. These distributions are sampled after the major eruptions have already been filled in by the exponential distributions in Table 1.

REFERENCES

Annan, J. D., J. C. Hargreaves, N. R. Edwards and R. Marsh (2005). "Parameter estimation in an intermediate complexity earth system model using an ensemble Kalman filter." Ocean Modelling **8**(1): 135-154 DOI: https://doi.org/10.1016/j.ocemod.2003.12.004.

Benhamou, E. (2018). "Kalman filter demystified: from intuition to probabilistic graphical model to real case in financial markets." arXiv e-prints **Statistical Finance (q-fin.ST)**(arXiv:1811.11618) DOI: https://doi.org/10.48550/arXiv.1811.11618.

Boltzmann, L. (1884). "Ableitung des Stefan'schen Gesetzes, betreffend die Abhängigkeit der Wärmestrahlung von der Temperatur aus der electromagnetischen Lichttheorie." Annalen der Physik **258**(6): 291-294 DOI: https://doi.org/10.1002/andp.18842580616.

Bouttier, F. (1996). Application of Kalman filtering to numerical weather prediction. Workshop on non-linear aspects of data assimilation, Shinfield Park, Reading, ECMWF.

Budyko, M. I. (1969). "The effect of solar radiation variations on the climate of the Earth." Tellus **21**(5): 611-619 DOI: 10.3402/tellusa.v21i5.10109.

Buizza, R., M. Milleer and T. N. Palmer (1999). "Stochastic representation of model uncertainties in the ECMWF ensemble prediction system." Quarterly Journal of the Royal Meteorological Society **125**(560): 2887-2908 DOI: https://doi.org/10.1002/qj.49712556006.

Carré, M., J. P. Sachs, J. M. Wallace and C. Favier (2012). "Exploring errors in paleoclimate proxy reconstructions using Monte Carlo simulations: paleotemperature from mollusk and coral geochemistry." Clim. Past **8**(2): 433-450 DOI: 10.5194/cp-8-433-2012.

Edwards, T. L., S. Nowicki, B. Marzeion, R. Hock, H. Goelzer, H. Seroussi, N. C. Jourdain, D. A. Slater, F. E. Turner, C. J. Smith, C. M. McKenna, E. Simon, A. Abe-Ouchi, J. M. Gregory, E. Larour, W. H. Lipscomb, A. J. Payne, A. Shepherd, C. Agosta, P. Alexander, T. Albrecht, B. Anderson, X. Asay-Davis, A. Aschwanden, A. Barthel, A. Bliss, R. Calov, C. Chambers, N. Champollion, Y. Choi, R. Cullather, J. Cuzzone, C. Dumas, D. Felikson, X. Fettweis, K. Fujita, B. K. Galton-Fenzi, R. Gladstone, N. R. Golledge, R. Greve, T. Hattermann, M. J. Hoffman, A. Humbert, M. Huss, P. Huybrechts, W. Immerzeel, T. Kleiner, P. Kraaijenbrink, S. Le clec'h, V. Lee, G. R. Leguy, C. M. Little, D. P. Lowry, J.-H. Malles, D. F. Martin, F. Maussion, M. Morlighem, J. F. O'Neill, I. Nias, F. Pattyn, T. Pelle, S. F. Price, A. Quiquet, V. Radić, R. Reese, D. R. Rounce, M. Rückamp, A. Sakai, C. Shafer, N.-J. Schlegel, S. Shannon, R. S. Smith, F. Straneo, S. Sun, L. Tarasov, L. D. Trusel, J. Van Breedam, R. van de Wal, M. van den Broeke, R. Winkelmann, H. Zekollari, C. Zhao, T. Zhang and T. Zwinger (2021). "Projected land ice contributions to twenty-first-century sea level rise." Nature **593**(7857): 74-82 DOI: 10.1038/s41586-021-03302-y.

Emile-Geay, J., N. P. McKay, D. S. Kaufman, L. von Gunten, J. Wang, K. J. Anchukaitis, N. J. Abram, J. A. Addison, M. A. J. Curran, M. N. Evans, B. J. Henley, Z. Hao, B. Martrat, H. V. McGregor, R. Neukom, G. T. Pederson, B. Stenni, K. Thirumalai, J. P. Werner, C. Xu, D. V. Divine, B. C. Dixon, J. Gergis, I. A. Mundo, T. Nakatsuka, S. J. Phipps, C. C. Routson, E. J. Steig, J. E. Tierney, J. J. Tyler, K. J. Allen, N. A. N. Bertler, J. Björklund, B. M. Chase, M.-T. Chen, E. Cook, R. de Jong, K. L. DeLong, D. A. Dixon, A. A. Ekaykin, V. Ersek, H. L. Filipsson, P. Francus, M. B. Freund, M. Frezzotti, N. P. Gaire, K. Gajewski, Q. Ge, H. Goosse, A. Gornostaeva, M. Grosjean, K. Horiuchi, A. Hormes, K. Husum, E. Isaksson, S. Kandasamy, K. Kawamura, K. H. Kilbourne, N. Koç, G. Leduc, H. W. Linderholm, A. M. Lorrey, V. Mikhalenko, P. G. Mortyn, H. Motoyama, A. D. Moy, R. Mulvaney, P. M. Munz, D. J. Nash, H. Oerter, T. Opel, A. J. Orsi, D. V. Ovchinnikov, T. J. Porter, H. A. Roop, C. Saenger, M. Sano, D. Sauchyn, K. M. Saunders, M.-S. Seidenkrantz, M. Severi, X. Shao, M.-

A. Sicre, M. Sigl, K. Sinclair, S. St. George, J.-M. St. Jacques, M. Thamban, U. Kuwar Thapa, E. R. Thomas, C. Turney, R. Uemura, A. E. Viau, D. O. Vladimirova, E. R. Wahl, J. W. C. White, Z. Yu, J. Zinke and P. A. k. Consortium (2017). "A global multiproxy database for temperature reconstructions of the Common Era." Scientific Data **4**(1): 170088 DOI: 10.1038/sdata.2017.88.

Feng, R., B. L. Otto-Bliesner, E. C. Brady and N. Rosenbloom (2020). "Increased Climate Response and Earth System Sensitivity From CCSM4 to CESM2 in Mid-Pliocene Simulations." Journal of Advances in Modeling Earth Systems **12**(8): e2019MS002033 DOI: https://doi.org/10.1029/2019MS002033.

Filar, J. A., P. S. Gaertner and M. A. Janssen (1996). An Application of Optimization to the Problem of Climate Change. State of the Art in Global Optimization: Computational Methods and Applications. C. A. Floudas and P. M. Pardalos. Boston, MA, Springer US**:** 475-498 DOI: 10.1007/978-1-4613-3437-8_29.

Forster, P., T. Storelvmo, K. Armour, W. Collins, J. L. Dufresne, D. Frame, D. J. Lunt, T. Mauritsen, M. D. Palmer, M. Watanabe, M. Wild and H. Zhang (2021). The Earth's Energy Budget, Climate Feedbacks, and Climate Sensitivity. Climate Change 2021: The Physical Science Basis. Contribution of Working Group I to the Sixth Assessment Report of the Intergovernmental Panel on Climate Change. V. Masson-Delmotte, P. Zhai, A. Pirani et al. Cambridge, United Kingdom and New York, NY, USA, Cambridge University Press**:** 923–1054 DOI: 10.1017/9781009157896.009.

Fujino, J., R. Nair, M. Kainuma, T. Masui and Y. Matsuoka (2006). "Multi-gas Mitigation Analysis on Stabilization Scenarios Using Aim Global Model." The Energy Journal **27**: 343-353.

Gettelman, A., C. Hannay, J. T. Bacmeister, R. B. Neale, A. G. Pendergrass, G. Danabasoglu, J. F. Lamarque, J. T. Fasullo, D. A. Bailey, D. M. Lawrence and M. J. Mills (2019). "High Climate Sensitivity in the Community Earth System Model Version 2 (CESM2)." Geophysical Research Letters **46**(14): 8329-8337 DOI: https://doi.org/10.1029/2019GL083978.

Grewal, M. S. and A. P. Andrews (2001). Kalman Filtering: Theory and Practice Using MATLAB, Wiley.

Gulev, S. K., P. W. Thorne, J. Ahn, F. J. Dentener, C. M. Domingues, S. Gerland, D. Gong, D. S. Kaufman, H. C. Nnamchi, J. Quaas, J. A. Rivera, S. Sathyendranath, S. L. Smith, B. Trewin, K. von Schuckmann and R. S. Vose (2021). Changing State of the Climate System. Climate Change 2021: The Physical Science Basis. Contribution of Working Group I to the Sixth Assessment Report of the Intergovernmental Panel on Climate Change. V. Masson-Delmotte, P. Zhai, A. Pirani et al. Cambridge, United Kingdom and New York, NY, USA, Cambridge University Press**:** 287–422 DOI: 10.1017/9781009157896.004.

Guttman, N. B. (1989). "Statistical Descriptors of Climate." Bulletin of the American Meteorological Society **70**(6): 602-607 DOI: 10.1175/1520-0477(1989)070<0602:SDOC>2.0.CO;2.

Harshvardhan and M. D. King (1993). "Comparative Accuracy of Diffuse Radiative Properties Computed Using Selected Multiple Scattering Approximations." Journal of the Atmospheric Sciences **50**(2): 247-259 DOI: 10.1175/1520-0469(1993)050<0247:caodrp>2.0.co;2.

Hijioka, Y., Y. Matsuoka, H. Nishimoto, T. Masui and M. Kainuma (2008). "Global GHG Emission Scenarios Under GHG Cconcentration Stabilization Targets." Journal of global environment engineering **13**: 97-108.

Hu, S. and A. V. Fedorov (2017). "The extreme El Niño of 2015-2016 and the end of global warming hiatus." Geophysical Research Letters **44**(8): 3816-3824 DOI: 10.1002/2017GL072908.

Jones, P. D. and C. Harpham (2013). "Estimation of the absolute surface air temperature of the Earth." Journal of Geophysical Research: Atmospheres **118**(8): 3213-3217 DOI: https://doi.org/10.1002/jgrd.50359.

Julier, S. J. and J. K. Uhlmann (1997). New extension of the Kalman filter to nonlinear systems. Proc.SPIE DOI: 10.1117/12.280797.

Kalman, R. E. (1960). "A New Approach to Linear Filtering and Prediction Problems." Journal of Basic Engineering **82**(1): 35-45 DOI: 10.1115/1.3662552.

Kalman, R. E. and R. S. Bucy (1961). "New Results in Linear Filtering and Prediction Theory." Journal of Basic Engineering **83**(1): 95-108 DOI: 10.1115/1.3658902.

Kaufman, D., N. McKay, C. Routson, M. Erb, B. Davis, O. Heiri, S. Jaccard, J. Tierney, C. Dätwyler, Y. Axford, T. Brussel, O. Cartapanis, B. Chase, A. Dawson, A. De Vernal, S. Engels, L. Jonkers, J. Marsicek, P. Moffa-Sánchez, C. Morrill, A. Orsi, K. Rehfeld, K. Saunders, P. S. Sommer, E. Thomas, M. Tonello, M. Tóth, R. Vachula, A. Andreev, S. Bertrand, B. Biskaborn, M. Bringué, S. Brooks, M. Caniupán, M. Chevalier, L. Cwynar, J. Emile-Geay, J. Fegyveresi, A. Feurdean, W. Finsinger, M.-C. Fortin, L. Foster, M. Fox, K. Gajewski, M. Grosjean, S. Hausmann, M. Heinrichs, N. Holmes, B. Ilyashuk, E. Ilyashuk, S. Juggins, D. Khider, K. Koinig, P. Langdon, I. Larocque-Tobler, J. Li, A. Lotter, T. Luoto, A. Mackay, E. Magyari, S. Malevich, B. Mark, J. Massaferro, V. Montade, L. Nazarova, E. Novenko, P. Pařil, E. Pearson, M. Peros, R. Pienitz, M. Płóciennik, D. Porinchu, A. Potito, A. Rees, S. Reinemann, S. Roberts, N. Rolland, S. Salonen, A. Self, H. Seppä, S. Shala, J.-M. St-Jacques, B. Stenni, L. Syrykh, P. Tarrats, K. Taylor, V. Van Den Bos, G. Velle, E. Wahl, I. Walker, J. Wilmshurst, E. Zhang and S. Zhilich (2020). "A global database of Holocene paleotemperature records." Scientific Data **7**(1) DOI: 10.1038/s41597-020-0445-3.

Kirtman, B., S. B. Power, A. J. Adedoyin, G. J. Boer, R. Bojariu, I. Camilloni, F. Doblas-Reyes, A. M. Fiore, M. Kimoto, G. Meehl, M. Prather, A. Sarr, C. Schär, R. Sutton, G. J. van Oldenborgh, G. Vecchi and H. J. Wang (2013). Near-term climate change. Projections and predictability, Cambridge University Press. **9781107057999:** 953-1028 DOI: 10.1017/CBO9781107415324.023.

Kopp, G. and J. L. Lean (2011). "A new, lower value of total solar irradiance: Evidence and climate significance." Geophysical Research Letters **38**(1) DOI: https://doi.org/10.1029/2010GL045777.

Kravitz, B., D. G. MacMartin, H. Wang and P. J. Rasch (2016). "Geoengineering as a design problem." Earth System Dynamics **7**(2): 469-497 DOI: 10.5194/esd-7-469-2016.

Kravitz, B., P. J. Rasch, H. Wang, A. Robock, C. Gabriel, O. Boucher, J. N. S. Cole, J. Haywood, D. Ji, A. Jones, A. Lenton, J. C. Moore, H. Muri, U. Niemeier, S. Phipps, H. Schmidt, S. Watanabe, S. Yang and J. H. Yoon (2018). "The climate effects of increasing ocean albedo: an idealized representation of solar geoengineering." Atmos. Chem. Phys. **18**(17): 13097-13113 DOI: 10.5194/acp-18-13097-2018.

Lacey, T. (1998). "Tutorial: The kalman filter." Computer Vision.

Lauritzen, S. L. (1981). "Time Series Analysis in 1880: A Discussion of Contributions Made by T.N. Thiele." International Statistical Review / Revue Internationale de Statistique **49**(3): 319-331 DOI: 10.2307/1402616.

Lauritzen, S. L. and T. N. Thiele (2002). Thiele: Pioneer in Statistics, Oxford University Press.

Lee, J. H. and N. L. Ricker (1994). "Extended Kalman Filter Based Nonlinear Model Predictive Control." Industrial and Engineering Chemistry Research **33**(6): 1530-1541 DOI: 10.1021/ie00030a013.

Lee, J. Y., J. Marotzke, G. Bala, L. Cao, S. Corti, J. P. Dunne, F. Engelbrecht, E. Fischer, J. C. Fyfe, C. Jones, A. Maycock, J. Mutemi, O. Ndiaye, S. Panickal and T. Zhou (2021). Future Global Climate: Scenario-Based Projections and Near-Term Information. Climate Change 2021: The Physical Science Basis. Contribution of Working Group I to the Sixth Assessment Report of the Intergovernmental Panel on Climate Change. V. Masson-Delmotte, P. Zhai, A. Pirani et al. Cambridge, United Kingdom and New York, NY, USA, Cambridge University Press**:** 553–672 DOI: 10.1017/9781009157896.006.

Lenssen, N. J. L., G. A. Schmidt, J. E. Hansen, M. J. Menne, A. Persin, R. Ruedy and D. Zyss (2019). "Improvements in the GISTEMP Uncertainty Model." Journal of Geophysical Research: Atmospheres **124**(12): 6307-6326 DOI: https://doi.org/10.1029/2018JD029522.

Livezey, R. E., K. Y. Vinnikov, M. M. Timofeyeva, R. Tinker and H. M. van den Dool (2007). "Estimation and Extrapolation of Climate Normals and Climatic Trends." Journal of Applied Meteorology and Climatology **46**(11): 1759-1776 DOI: 10.1175/2007JAMC1666.1.

Loeb, N. G., B. A. Wielicki, D. R. Doelling, G. L. Smith, D. F. Keyes, S. Kato, N. Manalo-Smith and T. Wong (2009). "Toward Optimal Closure of the Earth's Top-of-Atmosphere Radiation Budget." Journal of Climate **22**(3): 748-766 DOI: 10.1175/2008jcli2637.1.

MacMartin, D. G., B. Kravitz and D. W. Keith (2014). Geoengineering: The world's largest control problem. 2014 American Control Conference, IEEE.

Mann, M. E. (2008). "Smoothing of climate time series revisited." Geophysical Research Letters **35**(16) DOI: https://doi.org/10.1029/2008GL034716.

Marotzke, J. and P. M. Forster (2015). "Forcing, feedback and internal variability in global temperature trends." Nature **517**(7536): 565-570 DOI: 10.1038/nature14117.

McClelland, H. L. O., I. Halevy, D. A. Wolf-Gladrow, D. Evans and A. S. Bradley (2021). "Statistical Uncertainty in Paleoclimate Proxy Reconstructions." Geophysical Research Letters **48**(15): e2021GL092773 DOI: https://doi.org/10.1029/2021GL092773.

Meehl, G. A., R. Moss, K. E. Taylor, V. Eyring, R. J. Stouffer, S. Bony and B. Stevens (2014). "Climate Model Intercomparisons: Preparing for the Next Phase." Eos, Transactions American Geophysical Union **95**(9): 77-78 DOI: https://doi.org/10.1002/2014EO090001.

Merchant, C. J., O. Embury, C. E. Bulgin, T. Block, G. K. Corlett, E. Fiedler, S. A. Good, J. Mittaz, N. A. Rayner, D. Berry, S. Eastwood, M. Taylor, Y. Tsushima, A. Waterfall, R. Wilson and C. Donlon (2019). "Satellite-based time-series of sea-surface temperature since 1981 for climate applications." Scientific Data **6**(1) DOI: 10.1038/s41597-019-0236-x.

Miller, R. N. (1996). Introduction to the Kalman filter. Seminar on Data Assimilation, 2-6 September 1996, Shinfield Park, Reading, ECMWF.

Morice, C. P., J. J. Kennedy, N. A. Rayner and P. D. Jones (2012). "Quantifying uncertainties in global and regional temperature change using an ensemble of observational estimates: The

HadCRUT4 data set." Journal of Geophysical Research: Atmospheres **117**(D8) DOI: https://doi.org/10.1029/2011JD017187.

Morice, C. P., J. J. Kennedy, N. A. Rayner, J. P. Winn, E. Hogan, R. E. Killick, R. J. H. Dunn, T. J. Osborn, P. D. Jones and I. R. Simpson (2021). "An Updated Assessment of Near-Surface Temperature Change From 1850: The HadCRUT5 Data Set." Journal of Geophysical Research: Atmospheres **126**(3): e2019JD032361 DOI: https://doi.org/10.1029/2019JD032361.

Myers, M. A. and R. H. Luecke (1991). "Process control applications of an extended Kalman filter algorithm." Computers & Chemical Engineering **15**(12): 853-857 DOI: https://doi.org/10.1016/0098-1354(91)80030-Y.

Nasa/Larc/Sd/Asdc (2018). Global Space-based Stratospheric Aerosol Climatology Version 2.0.

Ogorek, B. (2019) "Yet Another Kalman Filter Explanation Article." Towards Data Science.

Okada, M., K. Yamanishi and N. Masuda (2020). "Long-tailed distributions of inter-event times as mixtures of exponential distributions." Royal Society Open Science **7**: 191643 DOI: 10.1098/rsos.191643.

Papale, P. (2018). "Global time-size distribution of volcanic eruptions on Earth." Scientific Reports **8**(1): 6838 DOI: 10.1038/s41598-018-25286-y.

Pielke Jr, R., M. G. Burgess and J. Ritchie (2022). "Plausible 2005–2050 emissions scenarios project between 2 °C and 3 °C of warming by 2100." Environmental Research Letters **17**(2): 024027 DOI: 10.1088/1748-9326/ac4ebf.

Rauch, H. E., F. Tung and C. T. Striebel (1965). "Maximum likelihood estimates of linear dynamic systems." AIAA Journal **3**(8): 1445-1450 DOI: 10.2514/3.3166.

Rodgers, K. B., S. S. Lee, N. Rosenbloom, A. Timmermann, G. Danabasoglu, C. Deser, J. Edwards, J. E. Kim, I. R. Simpson, K. Stein, M. F. Stuecker, R. Yamaguchi, T. Bódai, E. S. Chung, L. Huang, W. M. Kim, J. F. Lamarque, D. L. Lombardozzi, W. R. Wieder and S. G. Yeager (2021). "Ubiquity of human-induced changes in climate variability." Earth Syst. Dynam. **12**(4): 1393-1411 DOI: 10.5194/esd-12-1393-2021.

Ruggieri, E. and M. Antonellis (2016). "An exact approach to Bayesian sequential change point detection." Computational Statistics & Data Analysis **97**: 71-86 DOI: https://doi.org/10.1016/j.csda.2015.11.010.

Särkkä, S. (2013). Bayesian Filtering and Smoothing, Cambridge University Press.

Sato, M., J. E. Hansen, M. P. McCormick and J. B. Pollack (1993). "Stratospheric aerosol optical depths, 1850-1990." J. Geophys. Res. **98**: 22987-22994 DOI: 10.1029/93JD02553.

Schmidt, S. F. (1981). "The Kalman filter - Its recognition and development for aerospace applications." Journal of Guidance and Control **4**(1): 4-7 DOI: 10.2514/3.19713.

Schwartz, S. E. (2007). "Heat capacity, time constant, and sensitivity of Earth's climate system." Journal of Geophysical Research **112**(D24): D24S05-D24S05 DOI: 10.1029/2007JD008746.

Schwartz, S. E., n. Harshvardhan and C. M. Benkovitz (2002). "Influence of anthropogenic aerosol on cloud optical depth and albedo shown by satellite measurements and chemical transport modeling." Proceedings of the National Academy of Sciences **99**(4): 1784-1789 DOI: 10.1073/pnas.261712099.

Sellers, W. D. (1969). "A Global Climatic Model Based on the Energy Balance of the Earth-Atmosphere System." Journal of Applied Meteorology (1962-1982) **8**(3): 392-400.

Smith, S. W. (2003). Chapter 15 - Moving Average Filters. Digital Signal Processing. S. W. Smith. Boston, Newnes**:** 277-284 DOI: https://doi.org/10.1016/B978-0-7506-7444-7/50052-2.

Soden, B. J., R. T. Wetherald, G. L. Stenchikov and A. Robock (2002). "Global Cooling After the Eruption of Mount Pinatubo: A Test of Climate Feedback by Water Vapor." Science **296**(5568): 727-730 DOI: doi:10.1126/science.296.5568.727.

Stratonovich, R. L. (1959). "Optimum nonlinear systems which bring about a separation of a signal with constant parameters from noise." Radiofizika **2**(6): 892-901.

Stratonovich, R. L. (1960). "Application of the Markov processes theory to optimal filtering." Radio Engineering and Electronic Physics **5**(11): 1-19.

Susskind, J., G. A. Schmidt, J. N. Lee and L. Iredell (2019). "Recent global warming as confirmed by AIRS." Environmental Research Letters **14**(4): 044030 DOI: 10.1088/1748-9326/aafd4e.

Swerling, P. (1959). First-Order Error Propagation in a Stagewise Smoothing Procedure for Satellite Observations. Santa Monica, CA, RAND Corporation.

Tebaldi, C. and R. Knutti (2018). "Evaluating the accuracy of climate change pattern emulation for low warming targets." Environmental Research Letters **13** DOI: 10.1088/1748-9326/aabef2.

van Vuuren, D. P., M. G. J. den Elzen, P. L. Lucas, B. Eickhout, B. J. Strengers, B. van Ruijven, S. Wonink and R. van Houdt (2007). "Stabilizing greenhouse gas concentrations at low levels: an assessment of reduction strategies and costs." Climatic Change **81**(2): 119-159 DOI: 10.1007/s10584-006-9172-9.

Vernier, J., L. Thomason, J. P. Pommereau, A. Bourassa, J. Pelon, A. Garnier, A. Hauchecorne, L. Blanot, C. Trepte, D. Degenstein and F. Vargas (2011). "Major influence of tropical volcanic eruptions on the stratospheric aerosol layer during the last decade." GEOPHYSICAL RESEARCH LETTERS **38** DOI: 10.1029/2011GL047563.

Wan, E. A. and R. Van Der Merwe (2000). The unscented Kalman filter for nonlinear estimation, Institute of Electrical and Electronics Engineers Inc. DOI: 10.1109/ASSPCC.2000.882463.

Wang, Y. M., J. L. Lean and N. R. Sheeley, Jr. (2005). "Modeling the Sun's Magnetic Field and Irradiance since 1713." The Astrophysical Journal **625**: 522-538 DOI: 10.1086/429689.

Wielicki, B. A., B. R. Barkstrom, E. F. Harrison, R. B. Lee, G. Louis Smith and J. E. Cooper (1996). "Clouds and the Earth's Radiant Energy System (CERES): An Earth Observing System Experiment." Bulletin of the American Meteorological Society **77**(5): 853-868 DOI: 10.1175/1520-0477(1996)077<0853:catere>2.0.co;2.

Willner, D., C.-B. Chang and K.-P. Dunn (1977). Kalman filter algorithms for a multi-sensor system DOI: 10.1109/CDC.1976.267794.

Willson, R. C. and H. S. Hudson (1991). "The Sun's luminosity over a complete solar cycle." Nature **351**(6321): 42-44 DOI: 10.1038/351042a0.

Wunsch, C. (2020). "Is the Ocean Speeding Up? Ocean Surface Energy Trends." Journal of Physical Oceanography **50**(11): 3205-3217 DOI: 10.1175/jpo-d-20-0082.1.

Wunsch, C. and P. Heimbach (2007). "Practical global oceanic state estimation." Physica D: Nonlinear Phenomena **230**(1): 197-208 DOI: https://doi.org/10.1016/j.physd.2006.09.040.

Yang, S., Z. Li, J.-Y. Yu, X. Hu, W. Dong and S. He (2018). "El Niño–Southern Oscillation and its impact in the changing climate." National Science Review **5**(6): 840-857 DOI: 10.1093/nsr/nwy046.

Youngjoo, K. and B. Hyochoong (2018). Introduction to Kalman Filter and Its Applications. Introduction and Implementations of the Kalman Filter. G. Felix. Rijeka, IntechOpen DOI: 10.5772/intechopen.80600.

Zhong, W. and J. Haigh (2013). "The greenhouse effect and carbon dioxide." Weather **68**: 100-105 DOI: 10.1002/wea.2072.

Zhu, J., B. L. Otto-Bliesner, E. C. Brady, A. Gettelman, J. T. Bacmeister, R. B. Neale, C. J. Poulsen, J. K. Shaw, Z. S. McGraw and J. E. Kay (2022). "LGM Paleoclimate Constraints Inform Cloud Parameterizations and Equilibrium Climate Sensitivity in CESM2." Journal of Advances in Modeling Earth Systems **14**(4): e2021MS002776 DOI: https://doi.org/10.1029/2021MS002776.

SUPPLEMENT

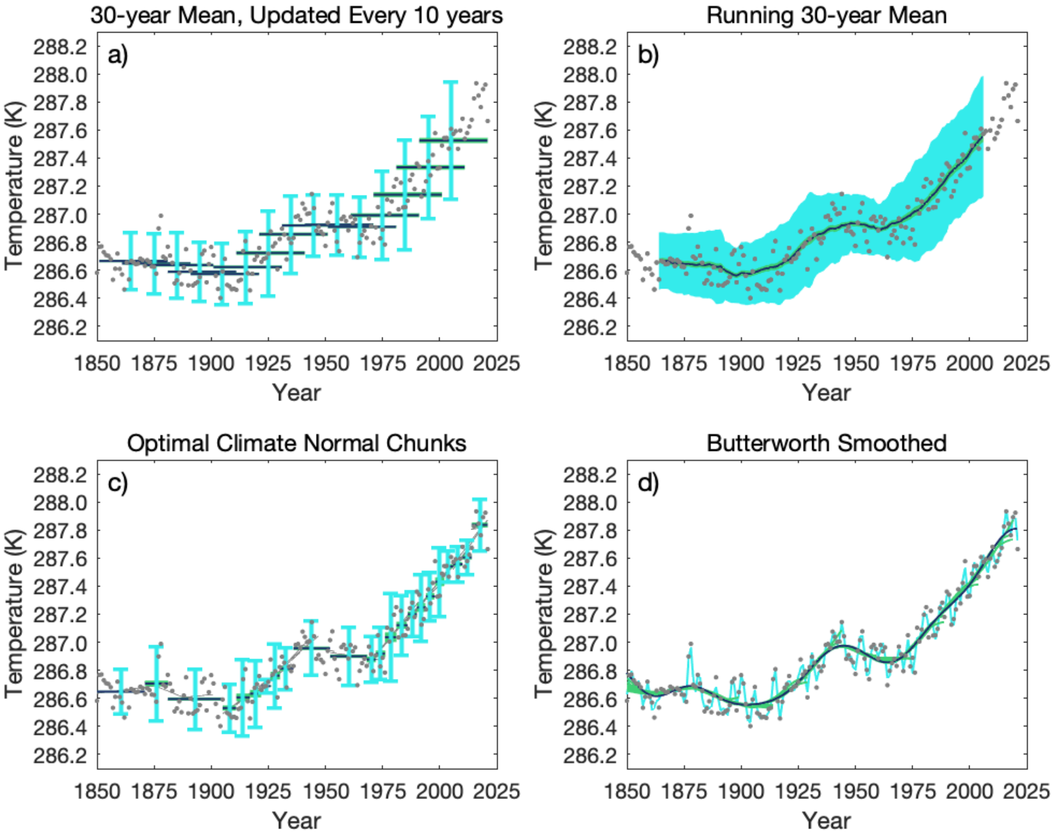

Supp. Fig. 1: Comparison of Prior Methods for Filtering or Smoothing the Climate as applied to the HadCRUT5 temperature dataset. (Morice, Kennedy et al. 2021) All metrics analogous to standard deviation are plotted at the 2σ level in light blue, and all metrics analogous to the standard error are plotted at the 1σ level in light green. a) The 30-year climate normals, updated every 10 years as per the World Meteorological Association in 1935. b) A running 30-year average. c) Adaptive periods of multiyear averages, known as the optimal climate normal (OCN). (Livezey, Vinnikov et al. 2007). Chunks became smaller as the rate of climate change increased in recent decades. d) The Butterworth Smoother applied to this temperature dataset. (Mann 2008) For the "standard error" highly smoothed lines, the lowpass adaptive, lowpass mean padded, and lowpass methods were applied to chunks of the timeseries data ranging from 50 to 170 years in increments of 15 years with a cutoff frequency of 1/30years. The black "best" line a lowpass adaptive curve extended to 2021. The blue "standard deviation" line is a lowpass mean padded filter with a cutoff frequency of 1/5years.

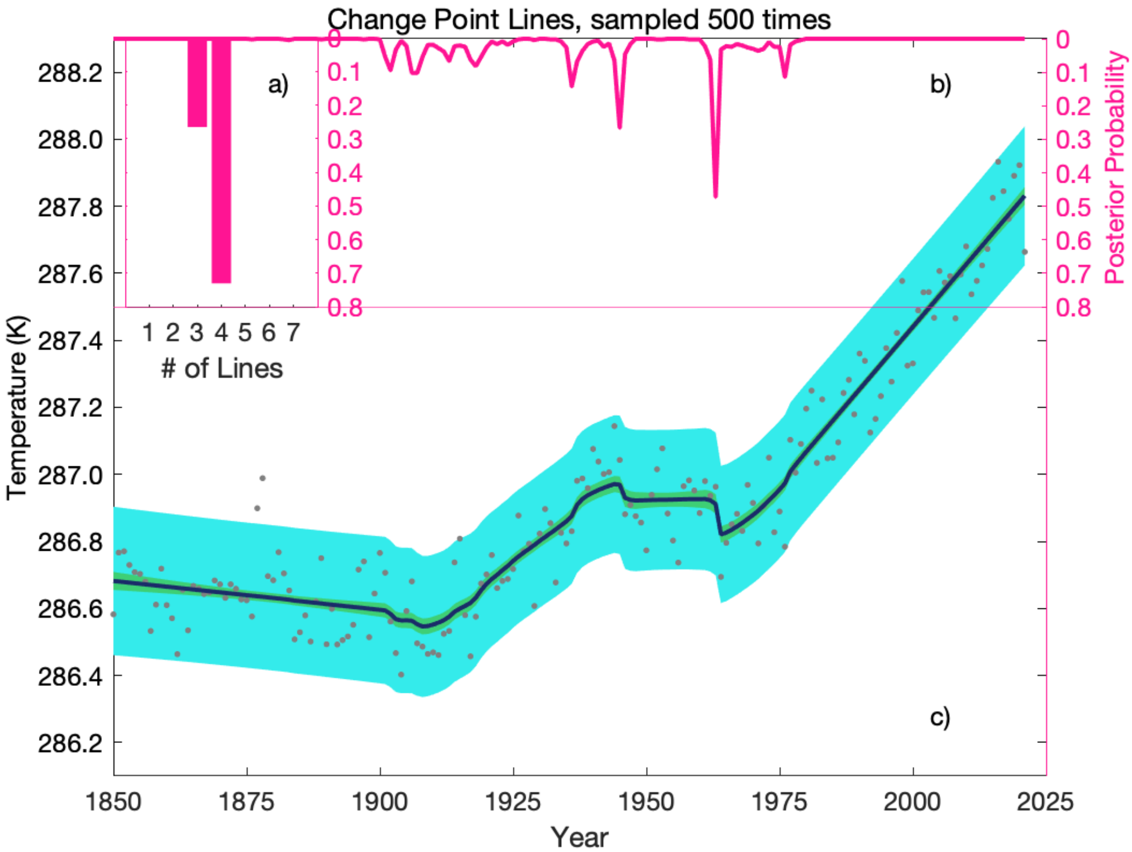

Supp. Fig. 2: Utilization of Bayesian Change Point on the HadCRUT5 data. (Ruggieri and Antonellis 2016) a) There are likely 4 trendlines with 73% of the posterior probability, and the remaining posterior probability on 3 trendlines. b) The posterior probability plot of where trendlines are most likely to occur: 50.4% of all samplings have a change point occur in 1963, and 25.2% of samplings have a change point occur in 1945. c) The posterior distribution of the trendlines in GMST, again with blue shading to indicate 2σ confidence interval of the data and green shading to indicate 1σ confidence interval of the mean trendline. These trend lines do not have to be continuous (note the dip at 1963), but over many samplings the trend becomes continuous.

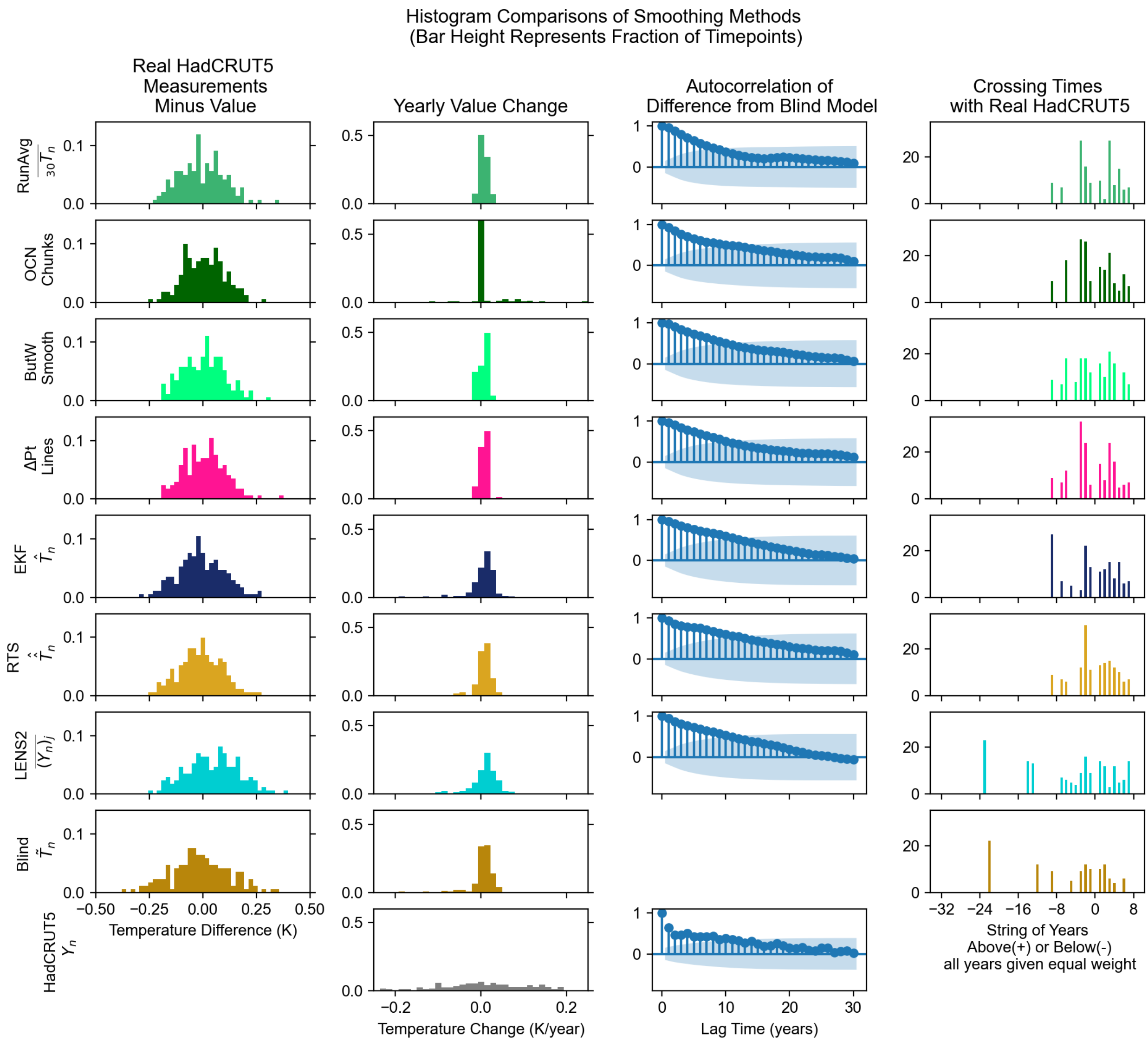

Supp. Fig. 3: Histogram comparisons of several aspects of many of the smoothing methods for generating a climate timeseries. The far-left column represents the absolute differences between the HadCRUT5 measurements and all the other models. All look similar in this respect. The center-left column shows the annual changes in the temperatures reported by each model. In this respect, the real HadCRUT5 measurements are the most spread out, because the stochastic change each year is large, whereas the in most years the OCN Chunks do not change. The center-right column shows an autocorrelation plot, which demonstrates that every other model aside from HadCRUT5 (and to a lesser extent the running average) are autocorrelated with the blind energy-balance model to similar degrees. The far-right column shows how many continuous years are spent above or below HadCRUT5: both the LENS2 ensemble average and the blind energy-balance model had >20 year spans for which they were colder than the "real" HadCRUT5 data, illustrating the benefit of data assimilation.

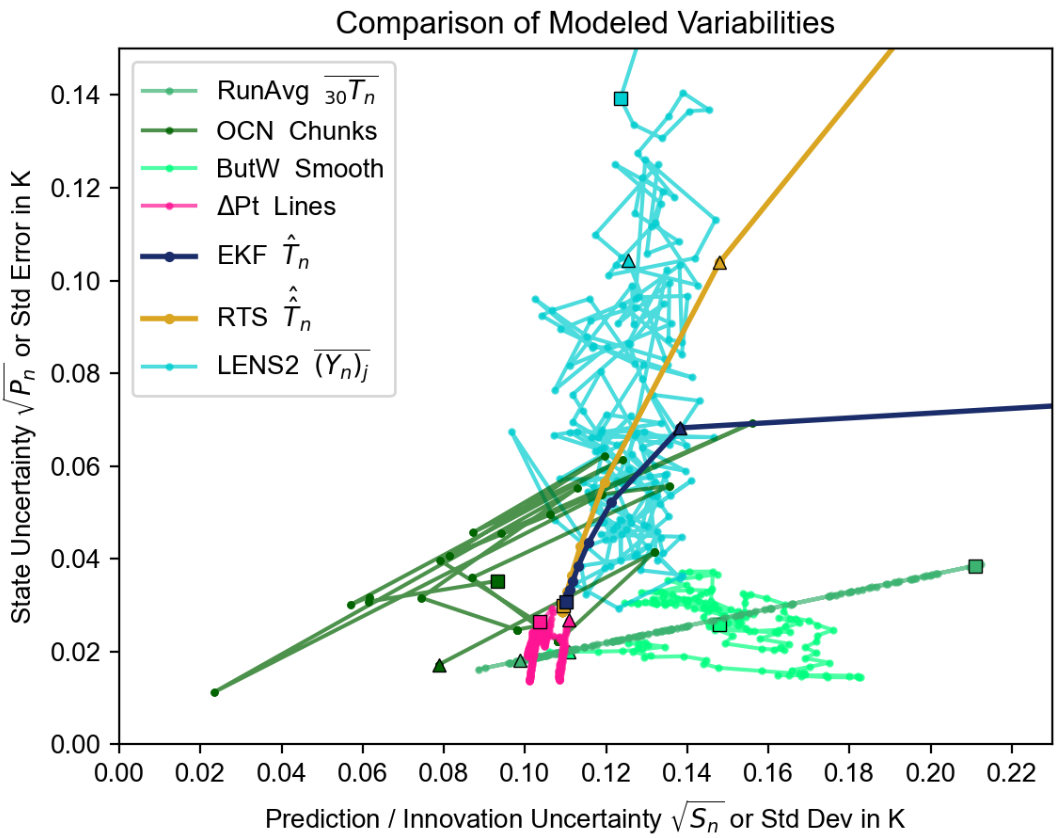

Supp. Fig. 4: Comparisons of the state and prediction (or equivalent) uncertainties of the smoothing methods for generating a climate timeseries. The x-axis represents the state uncertainty (colored light green in all other figures), and the y-axis represents the prediction uncertainty (colored light blue and doubled in all other figures). As these quantities change over time, all points in these smoothing timeseries are connected with colored lines, with the triangle △ representing the value of these quantities in 1850 or the first point that they entered the frame limits of this graph, and the square □ representing the value of these quantities in 2021 or the last point that they were within the frame limits. For instance, the running average draws a straight line because standard deviation and standard error are linearly correlated by a favor of 1/√30, and latter points have larger quantities for each variability due to the changing climate. The Butterworth Smoother traces a curve roughly in this region, with both the standard deviations and standard errors being twice the 15-year running average of the maximum of the absolute value of differences between colored and black curve. The RTS and EKF methods rapidly converge to a state uncertainty of ~0.110K and ~0.03K. The Change Point Regression variance also fluctuate in this region, although this methods' standard error twice drops to 0.014K. Both the OCN and the LENS2 climates have standard errors that are above the other methods at most times. For LENS2, the standard deviation within the CESM2 ensemble generally remains between 0.11K and 0.14K, whereas the state uncertainty is taken to be the standard deviation of the 20 ensembles comprising CMIP6 in October 2021. (Meehl, Moss et al. 2014) These metrics have nothing to do with Figure 10 in the main text. Within CMIP6, the 20 ensembles are most in agreement in 1939, when the state uncertainty dipped down to only 0.029K between ensemble means, but this uncertainty was much greater at earlier and later time points, reaching 0.183K by 2014.

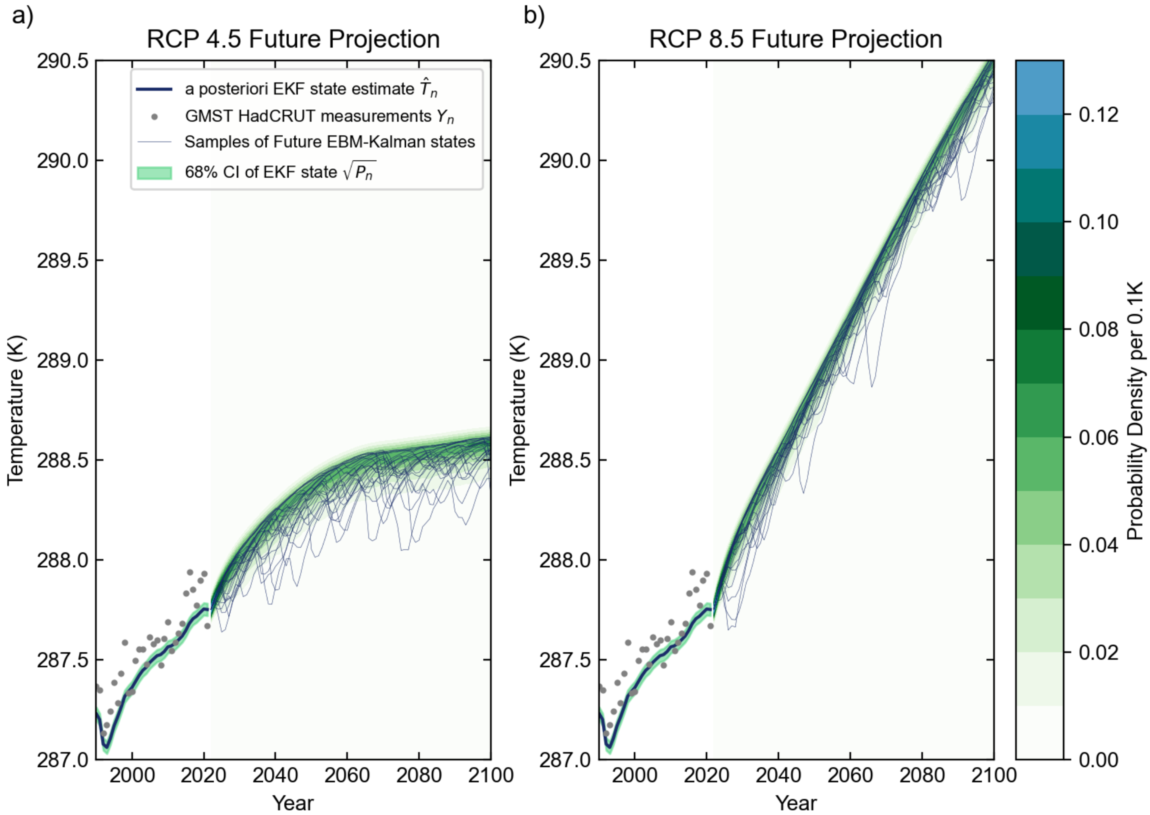

Supp. Fig. 5: Future projections of RCP4.5 (Supp. 5a) and RCP8.5 (Supp. 5a) scenarios using sampled measures of volcanic activity. This figure is identical to Fig. 6 in the main text, but utilizes the other two major RCPs for the CO_2 projection.